

AD-A279 906

## REPORT DOCUMENTATION PAGE



Public reporting burden for this collection of information is estimated to average 1 hour per response, including the time for reviewing instructions, searching existing data sources, gathering and maintaining the data needed, and completing and reviewing the collection of information. Send comments regarding this burden estimate or any other aspect of this collection of information, including suggestions for reducing this burden, to Washington Headquarters Services, Directorate for Information Operations and Reports, 1219 Jefferson Davis Highway, Suite 204, Arlington, VA 22202-4302, and to the Office of Management and Budget, Paperwork Reduction Project (0704-0188), Washington, DC 20503.

1. AGENCY USE ONLY (Leave blank)	2. REPORT DATE 4/28/94	3. REPORT TYPE AND DATES COVERED Final Technical Report: 8/15/92-3/31/94
----------------------------------	---------------------------	---

4. TITLE AND SUBTITLE (U) Heat Transfer, Fouling, and Combustion of Supercritical Fuels	5. FUNDING NUMBERS PE - 61102F PR - 2308 SA - BS G - F49620-92-J-0462
--	---

6. AUTHOR(S) L.D. Chen	8. PERFORMING ORGANIZATION REPORT NUMBER AFOSR-TR 94 0321
---------------------------	--

7. PERFORMING ORGANIZATION NAME(S) AND ADDRESS(ES) The University of Iowa Department of Mechanical Engineering Iowa City, IA 52242	9. SPONSORING/MONITORING AGENCY NAME(S) AND ADDRESS(S) AFOSR/NA 110 Duncan Avenue, Suite B115 Bolling AFB DC 20332-0001
---	--

10. SPONSORING/MONITORING AGENCY REPORT NUMBER S DTIC ELECTE JUN 06 1994 D
---

## SUPPLEMENTARY NOTES

S F D

## DISTRIBUTION/AVAILABILITY STATEMENT

Approved for public release; distribution is unlimited

## 12b. DISTRIBUTION CODE

## ABSTRACT (Maximum 200 words)

The specific objectives of the project were to investigate the dynamics of the vortex and flame interaction in jet diffusion flames and the transport phenomena associated with the injection of supercritical fluids into a sub-critical environment. The vortex-flame interaction in a near-laminar jet diffusion flame was quantified by a planar visualization and the vortex formation in a transitional jet diffusion flame by a line visualization. The measured vortex crossing frequency in transitional jet diffusion flames was used to verify the time-dependent diffusion flame calculations. The experiments also quantified the spray length in two different ambient environments composed of dissimilar species. The mixture pseudo-critical states were calculated for the conditions examined. The spray length, the calculated mixture pseudo-critical states, along with images of instantaneous light scattering and shadowgraph showed that the mixing of dense fluids dictated the spread of mist-like droplets and vapor-phase injector fluid. The supercritical sprays also exhibited flashing-like atomization as concluded from the experiments. Further investigation on the mixing in the supercritical sprays was suggested.

DTIC QUALITY INSPECTED A

14. SUBJECT TERMS Combustion, Jet Diffusion Flames, Sprays, Supercritical Sprays	15. NUMBER OF PAGES 65		
16. PRICE CODE			
17. SECURITY CLASSIFICATION OF REPORT Unclassified	18. SECURITY CLASSIFICATION OF THIS PAGE Unclassified	19. SECURITY CLASSIFICATION OF ABSTRACT Unclassified	20. LIMITATION OF ABSTRACT UL

**FINAL REPORT**

Approved for public release,  
distribution unlimited.

**HEAT TRANSFER, FOULING,  
AND COMBUSTION OF SUPERCRITICAL FUELS**

Contract Number: F49620-92-J-0462

Report Period: 15 August 1992 - 31 March 1994

**Submitted To**

**DIRECTORATE OF AEROSPACE SCIENCES (NA)  
AIR FORCE OFFICE OF SCIENTIFIC RESEARCH  
BOLLING AIR FORCE BASE, DC 20332-6448**

**By**

**Lea D. Chen  
Professor and Chair  
Department of Mechanical Engineering  
The University of Iowa  
Iowa City, Iowa 52242**

**Phone No.: 319/335-5674  
FAX No.: 319/335-5669**

**MARCH 1994**

## TABLE OF CONTENTS

	<u>Page</u>
I. INTRODUCTION .....	2
1.1. Project Summary .....	2
1.2. Personnel .....	2
1.3. List of Publications and Presentations .....	3
II. VORTEX-FLAME INTERACTION .....	4
III. NUMERICAL INVESTIGATION OF A JET DIFFUSION FLAME .....	5
IV. SUPERCRITICAL SPRAYS .....	6
4.1. Experimental Considerations .....	6
4.2. Results and Discussion .....	12
4.3. Uncertainty Estimate .....	23
4.4. Summary .....	24
APPENDIX A. VORTEX-FLAME INTERACTION .....	A-1
APPENDIX B. NUMERICAL INVESTIGATION OF A JET DIFFUSION FLAME .....	B-1

Accession For	
NTIS CRA&I	<input checked="" type="checkbox"/>
DTIC TAB	<input type="checkbox"/>
Unpublished	<input type="checkbox"/>
Justification .....	
By .....	
Distribution /	
Availability Codes	
Dist	Avail and/or Special
A-1	

## I. INTRODUCTION

### 1.1 Project Summary

The project period covers 15 August 1992 through 31 December 1994. The specific objectives are to investigate (1) the dynamics of the vortex and flame interaction in jet diffusion flames and (2) the transport phenomena of injection of supercritical fluids into a sub- or supercritical environment. The overall objective of the proposed project is to contribute to the Air Force in its effort of establishing a technology base for fuel and combustion systems to meet the requirements of future propulsion systems. The present research has emphasized on the dynamics of the transport processes, for example, regarding the vortex and flame (or flow) interaction and the injection of supercritical fluids into an environment which is composed of dissimilar fluids and maintained at subcritical states of the injected fluid.

This report is prepared to summarize the accomplishments during the project period, including (1) quantification of the vortex-flame interaction in a near-laminar jet diffusion flame, (2) verification of the numerical simulation of vortex structures inside a transitional jet diffusion flame, (3) experimental observation of supercritical sprays.

### 1.2 Personnel

The Project Director was L. D. Chen, Professor and Chairperson of the Department of Mechanical Engineering at The University of Iowa. During the early stage of the Project, K.-Y. Hsu served as a post-doctoral associate and conducted the experiments quantifying the vortex and flame interaction at Wright Laboratory. Hsu is presently a research scientist with Systems Research Laboratories-- a Division of Arvin/Calspan and is working at the Wright Laboratory. Two doctoral students, S. Lee (presently with Cummins Engine, Inc.) and H.-W. Lin (presently with Matusi-USA) were also funded during the initial period of the Project, and their doctoral degrees have been conferred. Two doctoral students are presently funded by the Project, P. Sui who is undertaking measurements to quantify the supercritical sprays and K.-Z. Jia who is working on the trapped vortex combustor- an innovative concept proposed by W. M. Roquemore of Wright Laboratory. Close collaboration with the Wright Laboratory has been accomplished

through the technical management of W. M. Roquemore.

### 1.3 List of Publications and Presentations

During the project period, an entry (for visualization of the vortex-flame interaction) to the 1992 Gallery of Fluid Flow of the Division of Fluid Dynamics, American Physical Society has been selected and published in Physics of Fluids A, (Hsu et al., 1993), a manuscript reporting the inner vortex crossing frequency will be submitted to a journal for publication (Lee et al., 1994). Two papers were presented in professional meetings to report the vortex-flame interactions (Hsu et al., 1993) and the chaotic aspects of the flame flicker in diffusion flames (Sui et al., 1993). Two Ph.D. dissertations were also completed. Lee (1992) reported the verification of the crossing frequency of the inner vortices in transitional jet diffusion flames and Lin (1993) reported the effects of the boundary conditions to the flicker phenomenon of a buoyant jet diffusion flame. A list of these publications follows.

#### Journal Articles

1. Hsu, K.-Y., Chen, L.-D., Katta, V. R., Goss, L. P., and Roquemore, W. M., 1993, "Flame-Vortex Interactions in a Driven Diffusion Flame," APS Physics of Fluids A, Fluid Dynamics (in Gallery of Fluid Motion), Vol. 30, p. S4.
2. Lee, S., Chen, L.-D. and Roquemore, W. M., 1994, "Vortex Crossing Frequency in a Transitional Jet Diffusion Flame," to be submitted to Combustion and Flame (1994).

#### Conference/Proceedings

1. Hsu, K. Y., Chen, L.-D., Katta, V.R., Goss, L.P., and Roquemore, W. M., 1993, "Experimental and Numerical Investigations of the Vortex-Flame Interactions in a Driven Jet Diffusion Flame," AIAA Paper 93-0455, Thirty-first Aerospace Science Meeting held in Reno, Nevada, 11-14 January, 1993.
2. Chen, L.-D., Sui, P.C., and Roquemore, W.M., 1993, "Dynamic Characteristics of a Buoyant Jet Diffusion Flame," Bulletin of the American Physical Society, Vol. 38, No. 10.

#### Thesis

1. Lee, S., "Flow-Flame Interaction of Nitrogen-Diluted Hydrogen Jet Diffusion Flame," Ph.D. Dissertation, Department of Mechanical Engineering, The University of Iowa, Iowa City, Iowa, December 1992.
2. Lin, H.-W., "Numerical Simulation of the Dynamics and Instability of Flame Flicker when Subject to Perturbed Boundary Conditions," Ph.D. Dissertation, Department of Mechanical Engineering, The University of Iowa, Iowa City, Iowa, December 1993.

## II. VORTEX-FLAME INTERACTION

The initial results of the vortex-flame interaction study are reported in a recent paper presented at the thirty-first Aerospace Science Meeting held in Reno, Nevada, 11-14 January, 1993 (Hsu et al., 1993). A specific type of the vortex-flame interaction is studied, in that the characteristic length of the vortex is much larger than the luminous flame thickness and the vortex characteristic time is much longer than the reaction characteristic time. This vortex was formed due to an acoustic driving to the fuel jet (in a co-flowing air environment) at 30 Hz. The acoustic driving periodically reproduces a large ring vortex, and an accompanying counter-rotating ring-vortex pair. These large ring vortices interact with the thin flame typical of a near-laminar jet diffusion flame. This interaction leads to local extinction through stretched flame characteristics. The preliminary data obtained thus far suggest that partial premixing may have occurred inside the ring vortex pair. It also suggests that convoluted flame sheets or distributed reactions may exist in the vortex pair. The above speculation needs to be confirmed by experiments. The preprint of the paper by Hsu, et al. (1993) is included in Appendix A.

### III. NUMERICAL INVESTIGATION OF A JET DIFFUSION FLAME

A manuscript (Lee et al., 1994) quantifying the crossing frequency of the inner vortices and verification of the numerical simulation has been prepared and will be submitted for publication in an archival journal. The crossing frequency of the inner vortex in a transitional jet diffusion flame was measured as a function of axial location using a line-visualization technique. Step-wise decreases of the crossing frequency were observed in the experiments, in qualitative agreement with that reported in the literature. The numerical simulation based on a simple flame-sheet model was shown to reproduce the inner vortex in the transitional jet diffusion flame studied. Random perturbations applied at the fuel-jet exit were required for the prediction of roll-up vortices inside the flame. The simulation results also revealed a step-wise decrease of the crossing frequency along the axial direction. The simulation, although captured the major components of the crossing frequency in the jet near field, was only in qualitative agreement with the experimental crossing frequency data as a function of axial location. The Strouhal number scaling of the vortex crossing frequency showed that the Strouhal number was bounded by 0.2 and 1.0, typical of the Kelvin-Helmholtz instability of cold jets. The results obtained during the project period suggested that the inner vortex is a Kelvin-Helmholtz type of the convective instability which is modified due to the presence of the high-temperature flame zone. The two-dimensional numerical model, therefore, is capable of reproducing the frequency characteristics of the buoyancy-induced vortex in transitional jet diffusion flames as well as capturing the frequency components of a Kelvin-Helmholtz type of instability inside the flame. A copy of the manuscript of Lee et al. (1994) is included in Appendix B.

## IV. SUPERCRITICAL SPRAYS

### 4.1 Experimental Considerations

The injection of high-pressure sprays (i.e., the injected fluid pressure being around or higher than its thermodynamic critical pressure) can be cataloged, for example, into three regimes: high pressure sprays (Regime 1), supercritical sprays (Regime 2) and supercritical flashing injection (Regime 3), shown in the temperature-entropy diagram (or T-s diagram) of Fig. 1. If one considers the spray into an environment being composed of its own vapor, the T-s diagram shown in Fig. 1 adequately describes the spray regimes. Regime 1 signifies such a typical fuel injection condition in a diesel engine or in a conventional jet engine. The fuel at the injector exit usually has a supercritical pressure but a sub-critical temperature. Therefore, the atomization and vaporization is crucial to the mixing of this injection process. In Regime 2, the injector fluid is typically supercritical (but near-critical). For a single-component system, the mixing of dense fluids dictates the transport process. However, when a dissimilar fluid or a multi-component system (such as the combustor condition) is involved, the thermodynamic state varies as the local mixing condition varies. For example, the local thermodynamic critical pressure and temperature are to be determined by the local multi-component phase equilibrium when the injector fluid is in contact with a dissimilar fluid. It is, therefore, conceivable that the mixing of a supercritical fluid with a dissimilar fluid can result in recondensation of the injector fluid when the local phase equilibrium is maintained. The transport of the injector supercritical fluid, however, should determine the local mixture states. The injection process in Regime 2 yields a mixture thermodynamic state located in the liquid side of the two-phase dome. The injection process of a supercritical fluid, however, can also result in a flashing injection when the mixture thermodynamic state is located in the vapor side of the two-phase dome, for example, Regime 3 of Fig. 1. The flashing injection can be achieved when the injector fluid has an excess enthalpy (or having a higher temperature) exceeding the enthalpy of vaporization of the mixture. This concept was explored by Szetela and TeVelde (1982) and termed external fuel vaporization for aircraft gas turbines. The injection of a supercritical fluid into a dissimilar fluid environment is the focus of the present study.

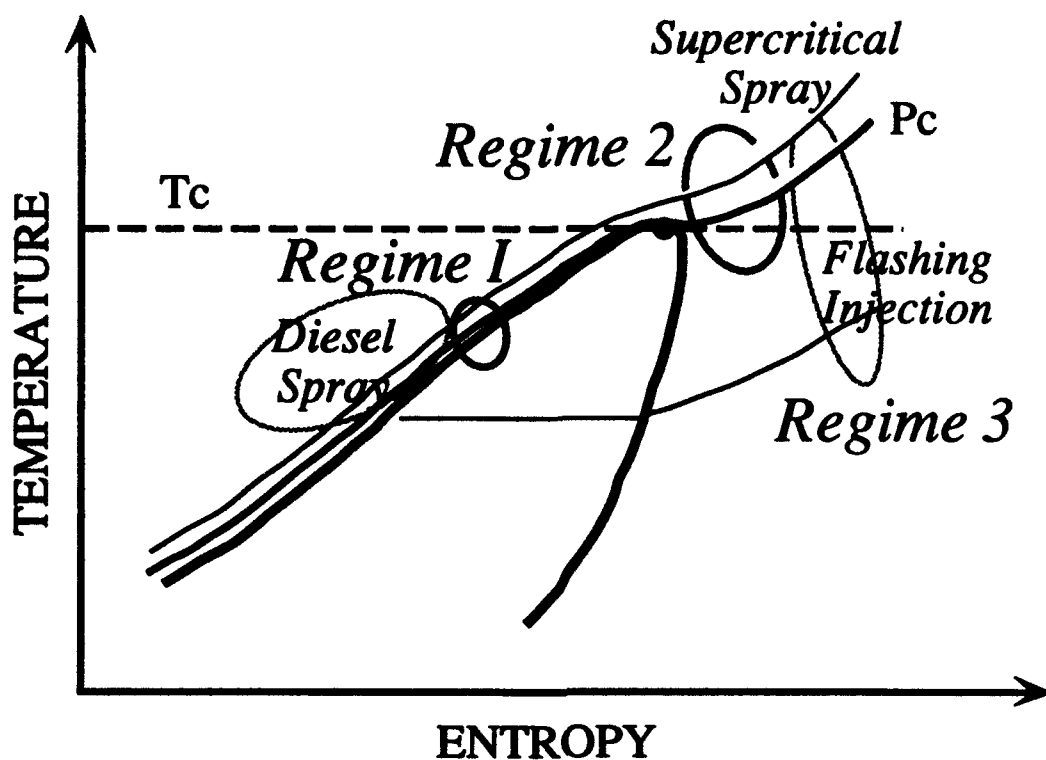


Figure 1. A Schematic of High-Pressure Spray Regimes

A simulant fluid, SF<sub>6</sub> (Matheson SCF purity grade), is employed to study the injection process. This fluid is non-toxic, nonflammable, and environmentally friendly, and it also has properties similar to typical hydrocarbon fuels. Some noted properties are its molecular weight, the near critical-state dynamic viscosity and density. Therefore, this simulant fluid makes a good candidate fluid to study the injection process of liquid fuels. The critical temperature and pressure of SF<sub>6</sub> are, respectively, 318.7 K and 37.1 bar, and those of typical hydrocarbon fuels are 700 K and 20 bars. Therefore, the heating requirement to bring SF<sub>6</sub> to a supercritical state is less demanding than that to bring hydrocarbon fuels to a similar thermodynamic state.

The experimental set-up includes a fuel delivery system, a spray nozzle, and a high-pressure spray chamber (e.g., see Fig. 2). A HPLC pump (Gilson 305 Piston Pump, with pump head Model 50SC) is used to deliver the injector fluid at preset flow rates. The pump pressure, however, can not be accurately pre-set because it is determined by the pressure drop needed to deliver the desired flow rate at the chamber pressure. The high-pressure chamber (American

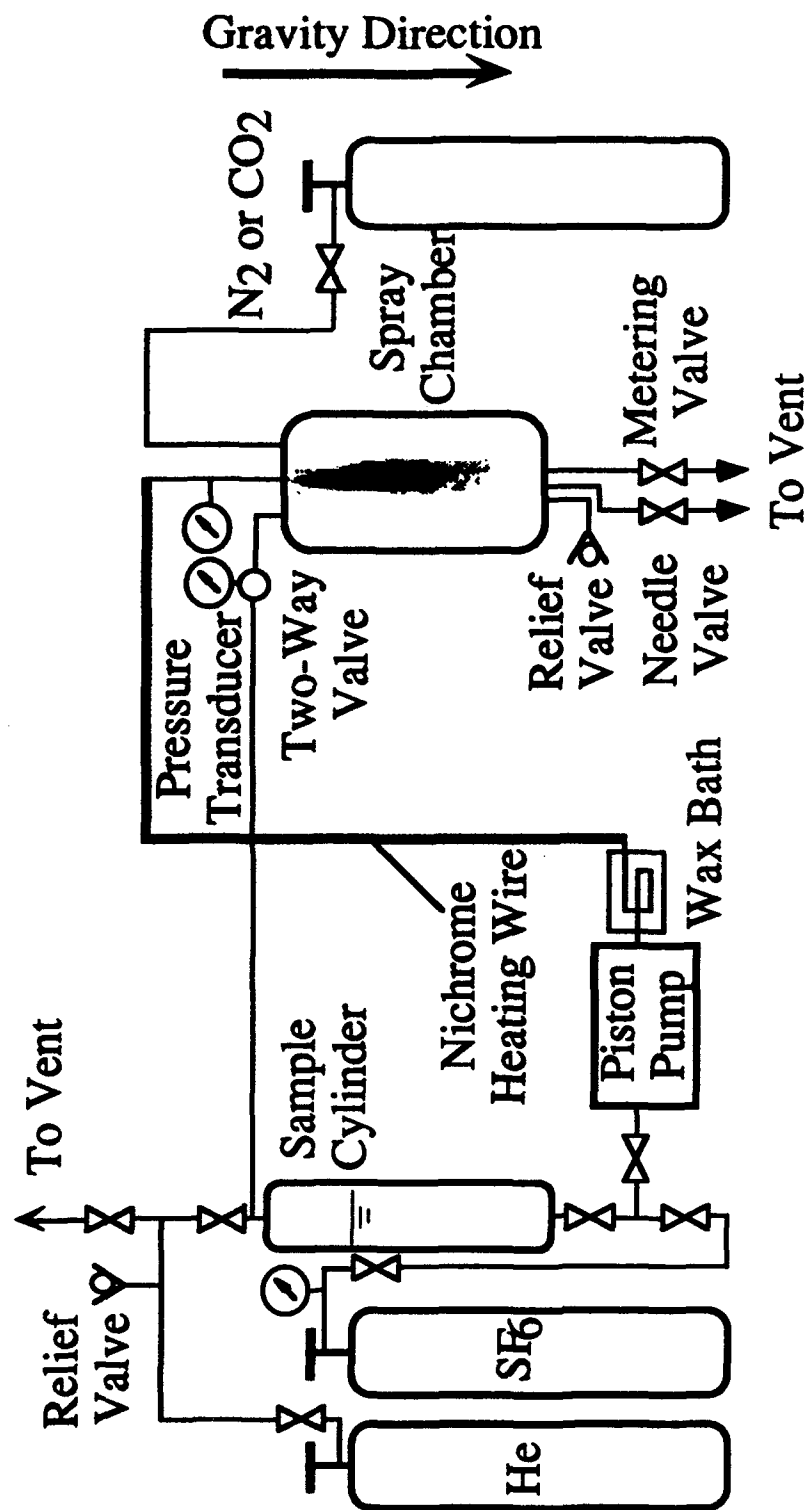


Figure 2. A Schematic of Experimental Set-up

Research Corporation) has an inside diameter of 102 mm and height of 430 mm. The total volume of the chamber is approximately  $3.6 \times 10^{-3} \text{ m}^3$ . Four gauge glasses are mounted on the chamber, each separates by 90 degrees. The high pressure chamber is designed for operation with a pressure as high as 68 bars (Roquemore, 1992). Prior to the injector exit, the SF<sub>6</sub> is heated by a wax bath, with a heating tape wrapped around the stainless steel tubing. A near-critical temperature is maintained at the injector exit as can be seen from the reduced temperature (Tr) shown in Table 1. Two spray injectors have been used, one is a commercially available pressure atomizer (Spraying System 17530-SS005) with a specified orifice size (127  $\mu\text{m}$  in diameter) and the other was a Wright Laboratory designed and manufactured glass injector (Switzer, 1992). The glass nozzle has a long passage of  $l/d_i$  equal to 36 ( $l$  being the passage length and  $d_i$  the inside diameter) and a sudden contraction prior to the nozzle exit; the contraction ratio  $d_i/d_e$  is equal to 6,  $d_e$  being the injector diameter. The diameter of this nozzle is estimated to be 150  $\mu\text{m}$ . The nozzle is installed vertically in the top center of the chamber. A sub-miniature k-type thermocouple (Omega KMQSS-020E) is inserted into the nozzle assembly at about 20 mm upstream of the nozzle exit.

The SF<sub>6</sub> was injected into the spray chamber filled with N<sub>2</sub> (designated as SF<sub>6</sub>/N<sub>2</sub>), CO<sub>2</sub> (designated as SF<sub>6</sub>/CO<sub>2</sub>), or its own vapor (designated as SF<sub>6</sub>/SF<sub>6</sub>). The SF<sub>6</sub>/SF<sub>6</sub> condition serves as a reference for the flashing injection of a supercritical fluid. The mass flow rate of SF<sub>6</sub> is maintained constant,  $3.75 \times 10^{-4} \text{ kg/s}$ , through the tests. It should be noted that there is no throttling process in the flow passage after the pump. Wax bath and/or heating tape, or nichrome wire are used to heat the SF<sub>6</sub>. The test chamber is charged by CO<sub>2</sub>, N<sub>2</sub>, or SF<sub>6</sub> vapor as the ambient gas to desired pressures prior to the experiments. A small amount of the ambient gas is allowed to flow through the chamber during the tests. The chamber pressure is maintained constant and is controlled by adjusting the fine metering valve at the bottom of the chamber. The test conditions are summarized in Table 1. The test conditions are determined by maintaining a same volumetric flow rate (mass flow rate) for the injection conditions. Therefore, a direct comparison of droplet formation (recondensation) and spray length can be made. The volumetric

flow rate is determined to yield a turbulent Reynolds number ( $Re$ ) at the injector exit and a spray in the atomization regime following the jet breakup regime boundaries, for example, summarized and defined by Reitz and Bracco (1986). The spray regime is identified by the Ohnesorge (Oh) and Reynolds numbers based on the injector exit condition. The Froude number (Fr) of the test conditions is in the range  $7.3 \times 10^{-7}$  to  $3.3 \times 10^{-6}$ , suggesting that these conditions are momentum dominated. The chamber is maintained with a near-critical pressure as can be seen from the dimensionless pressure ( $Pr'$ ), which is normalized by the critical pressure of SF<sub>6</sub> shown in Table 1. The dimensionless pressure of the chamber,  $Pr'$ , is also the reduced pressure of SF<sub>6</sub> at the injector exit. It should be mentioned that no heating is applied to the chamber. Therefore, the chamber is assumed to be at room temperature (or 298 K) for all the conditions, or having a corresponding reduced temperature based on the SF<sub>6</sub> critical temperature ( $Tr'$ ) of 0.92.

Two diagnostic techniques are employed, "planar" imaging and shadowgraph visualization. The "planar" imaging was accomplished by passing through the center of the spray with a vertical laser sheet. A He-Ne laser (10 mW at 632 nm) is used as the illuminating laser source. The spray image is recorded by a CCD video camera (Cannon A-1, or Panasonic AG-180U) which is positioned normal to the illuminating light sheet. The video image is digitized by a frame grabber (Scion Image Capture II; 8-bit resolution) interfaced to a micro-computer (Mac IIx) for analysis and measurements of the spray length. Limited experiments are conducted using a pulsed (10 ns) Nd:YAG laser (wavelength at 532 nm) as the illuminating light source to resolve the instantaneous flow features. The Nd:YAG laser is used in conjunction with an intensified CCD (ICCD) camera positioned normal to the illuminating light sheet. The ICCD camera is based on a commercial unit (Photometrics Model CH220/camera head and Thomson TH7882 CCD chip, 384 x 576 pixels) with a fiber-optically bonded intensifier (ITT Model F4111 S-20 intensifier).

The thickness of the illuminating laser sheet is about 250  $\mu\text{m}$  in thickness. This thickness can not provide spatially-resolved results of the near-field imaging because of being on the similar order of magnitude of the injector diameter (around 130  $\mu\text{m}$ ). Therefore, "light scattering" instead of "planar" imaging will be used in the discussion. To assist interpretation of the "light scattering"

Table 1. Summary of Experimental Condition

	SF6-N2	SF6-CO2	SF6-SF6
d ( $\mu\text{m}$ )	127 (Delevan Nozzle); 150 (WL Nozzle)		
Vol. Flowrate ( $\text{m}^3/\text{s}$ )	$2.5 \times 10^{-7}$	$2.5 \times 10^{-7}$	
Mass Flowrate ( $\text{kg/s}$ )	$3.75 \times 10^{-4}$	$3.75 \times 10^{-4}$	
Tr	0.92 - 1.01	0.92 - 1.01	0.92 - 1.01
Pr'	0.9 - 1.1	0.9 - 1.1	0.9 - 1.1
Re	29000 - 155000	29000 - 155000	
We	23500 - $\infty$	23500 - $\infty$	
Oh (Ohnesorge No.)	$5.1 \times 10^{-3} - \infty$	$5.1 \times 10^{-3} - \infty$	
Fr	$7.3 \times 10^{-7} - 3.3 \times 10^{-6}$	$7.3 \times 10^{-7} - 3.3 \times 10^{-6}$	
FN (Flow Number)	$\left( \frac{\dot{m}^2}{\rho \Delta p} \right)$ $2.5 \times 10^{-8} - 6.5 \times 10^{-8}$		

results, shadowgraph images are taken using both the He-Ne laser as the light source.

#### 4.2 Results and Discussion

The light scattering image is used to determine the "spray penetration length" (or the spray length). The video image is digitized by a frame grabber (8-bit dynamic range). Ten randomly selected frames are used to obtain averaged intensities. Typical axial intensity profiles are shown in Fig. 3 for SF<sub>6</sub> injection into N<sub>2</sub> with an injector exit temperature of Tr = 0.95, 0.96, 0.97, 0.98, 0.99 or 1.00. The chamber is maintained at Pr' = 1.0. The normalized light intensity shown in Fig. 3 is based on an 8-bit dynamic range, i.e., 255 being the highest intensity and 0 the lowest. The measured intensity decreases as the axial distance is increased, a result of the decreasing light scattering cross-section due to the decrease of droplet size or droplet number density (or both).

Based on a threshold value of 5, the measured spray length plotted in l/d (l being the spray length and d the nozzle diameter) is shown in Fig. 4. The spray length decreases with increasing Tr for SF<sub>6</sub> injection into CO<sub>2</sub> and N<sub>2</sub> environments. Three chamber pressures, Pr' = 0.9, 1.0 and 1.1, are examined in the experiments. The spray length is shorter for lower chamber pressures, particularly true for the injection into N<sub>2</sub> environment.

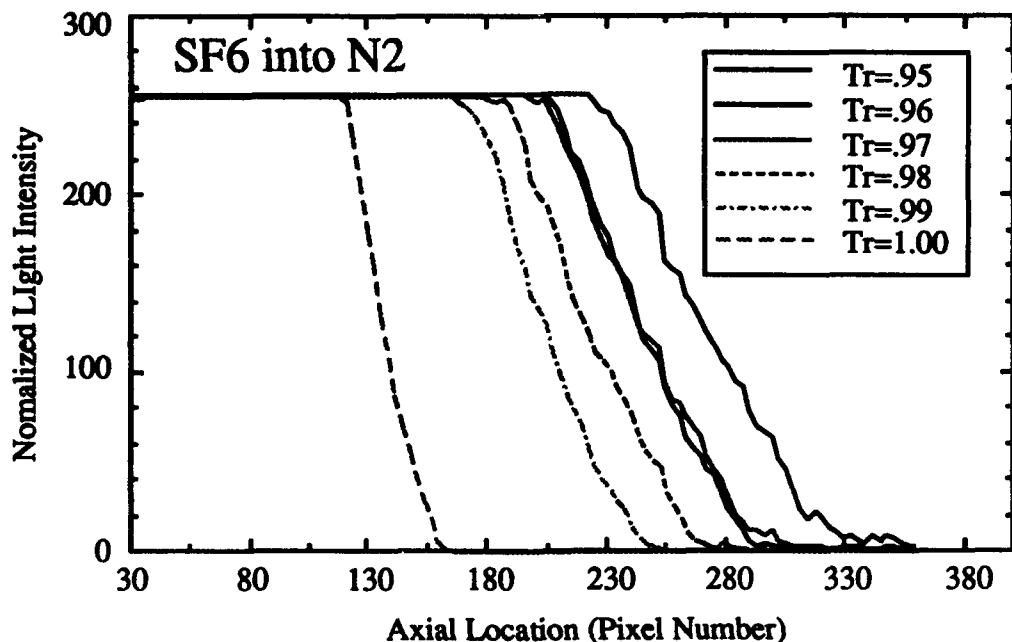


Figure 3. Axial Profiles of Scattered Light Intensity.

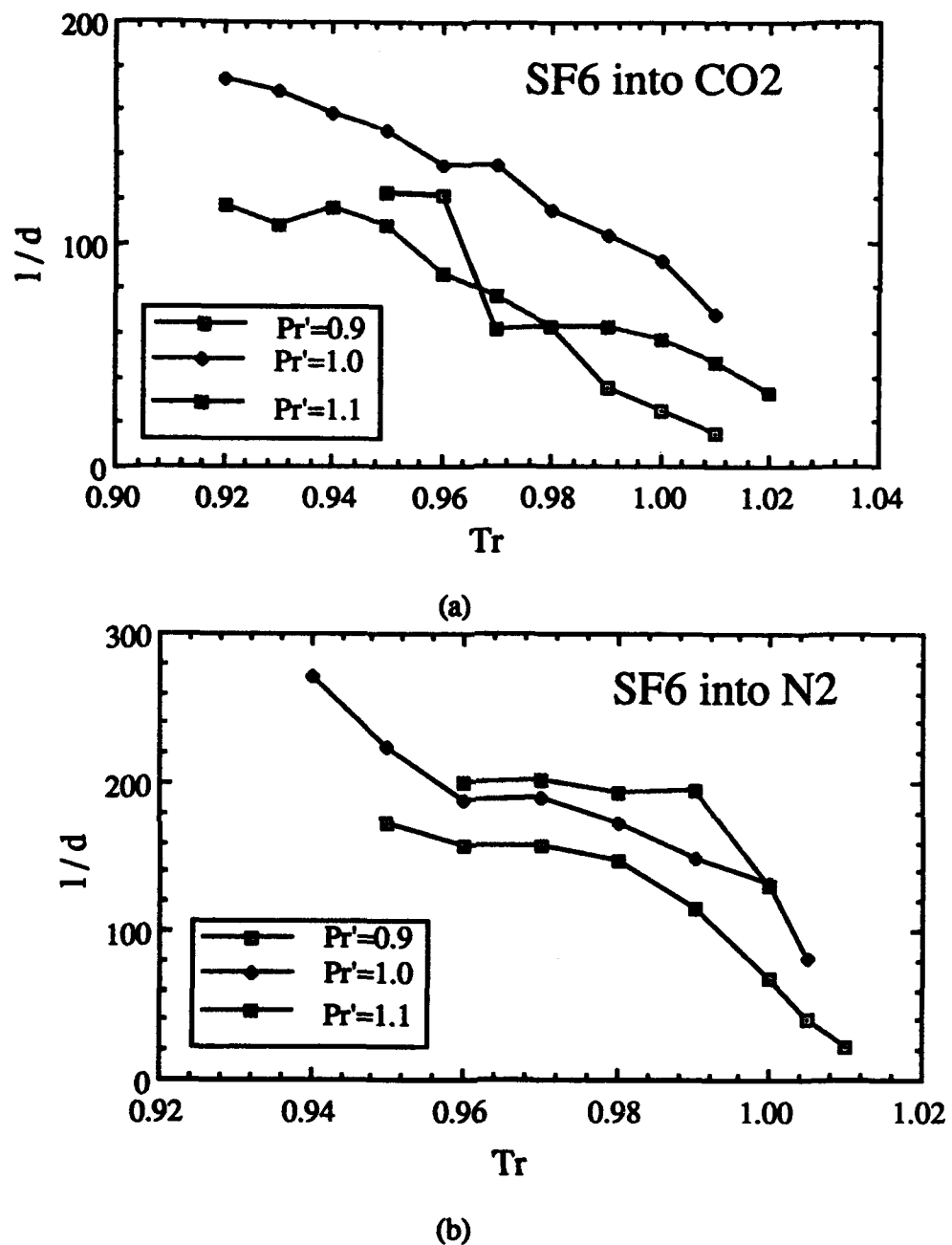


Figure 4. Dimensionless Spray Length Versus Tr; (a) SF<sub>6</sub> into CO<sub>2</sub> and (b) SF<sub>6</sub> into N<sub>2</sub>.

To assist interpretation of the measured spray length, a parabolic flow calculation based on the locally homogeneous flow (LHF) model assumption in conjunction with a  $k-\epsilon-g$  turbulence model is performed. The  $SF_6$  density as a function of  $Tr$  is shown in Fig. 5 for three pressures,  $Pr = 0.9, 1.0$ , and  $1.1$ . The density decreases rapidly when the critical temperature is approached. The calculated potential core length ( $l_p$ ) using a GENMIX-based computer program is shown in Fig. 6 for injection of near and supercritical  $SF_6$  into  $CO_2$  and  $N_2$  environments at conditions similar to the experiments. The predicted potential core, shown in Fig. 6, decreases with increasing temperature. When temperature is increased, the density of  $SF_6$  decreases so does the density ratio of  $SF_6$  to  $N_2$  or  $CO_2$ . It is this decrease in density ratio that yields a shorter potential core. The measured spray penetration length (Fig. 4) shows a decreasing trend similar to that of the predicted potential core (Fig. 6). This comparison suggests that the mixing of dense fluids should be investigated in the study of injection of supercritical fluids.

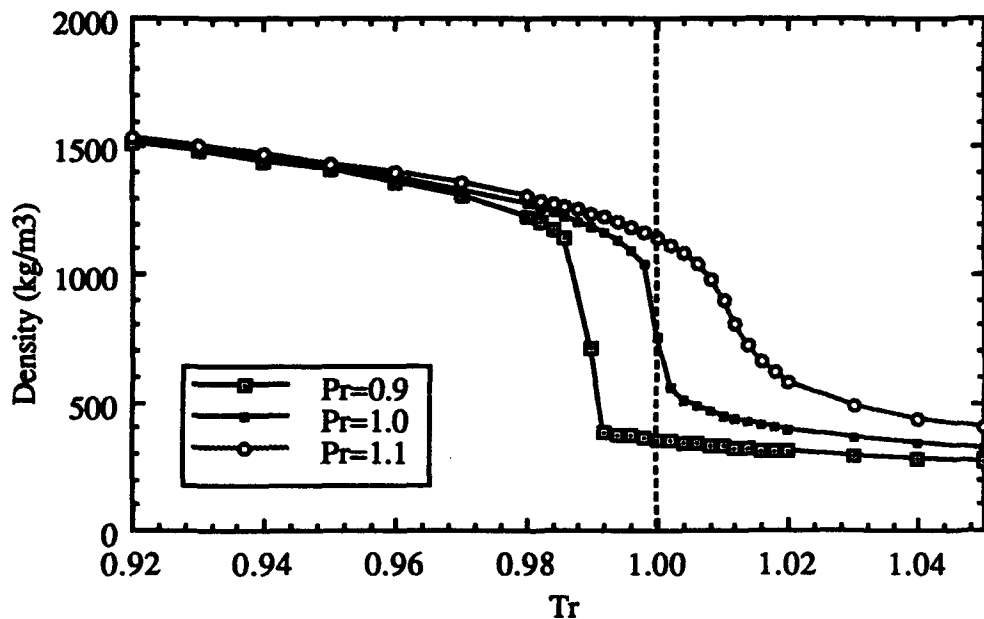


Figure 5. Density of  $SF_6$  versus  $Tr$

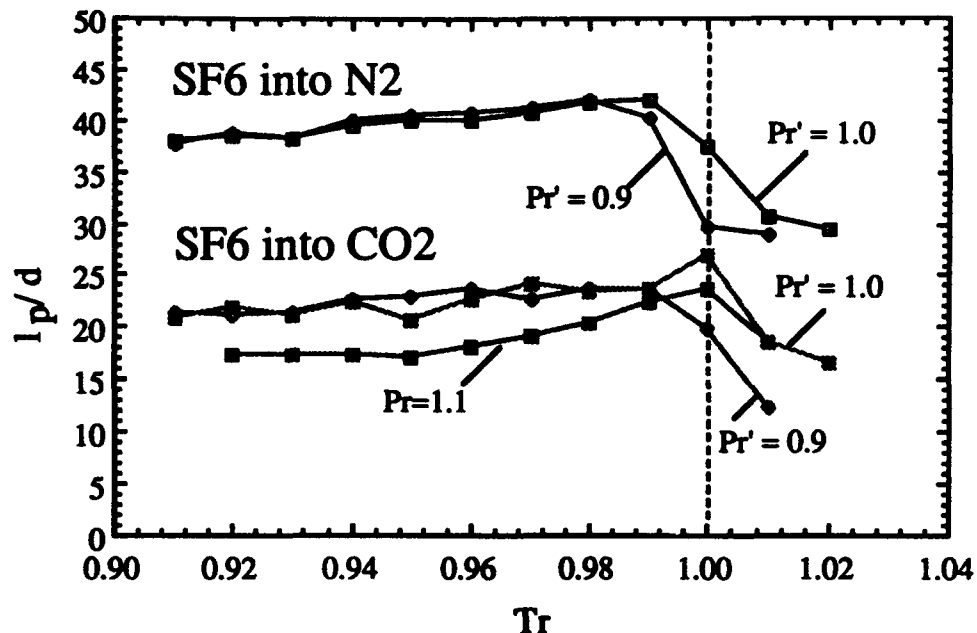


Figure 6. LHF Calculation of Potential Core Length

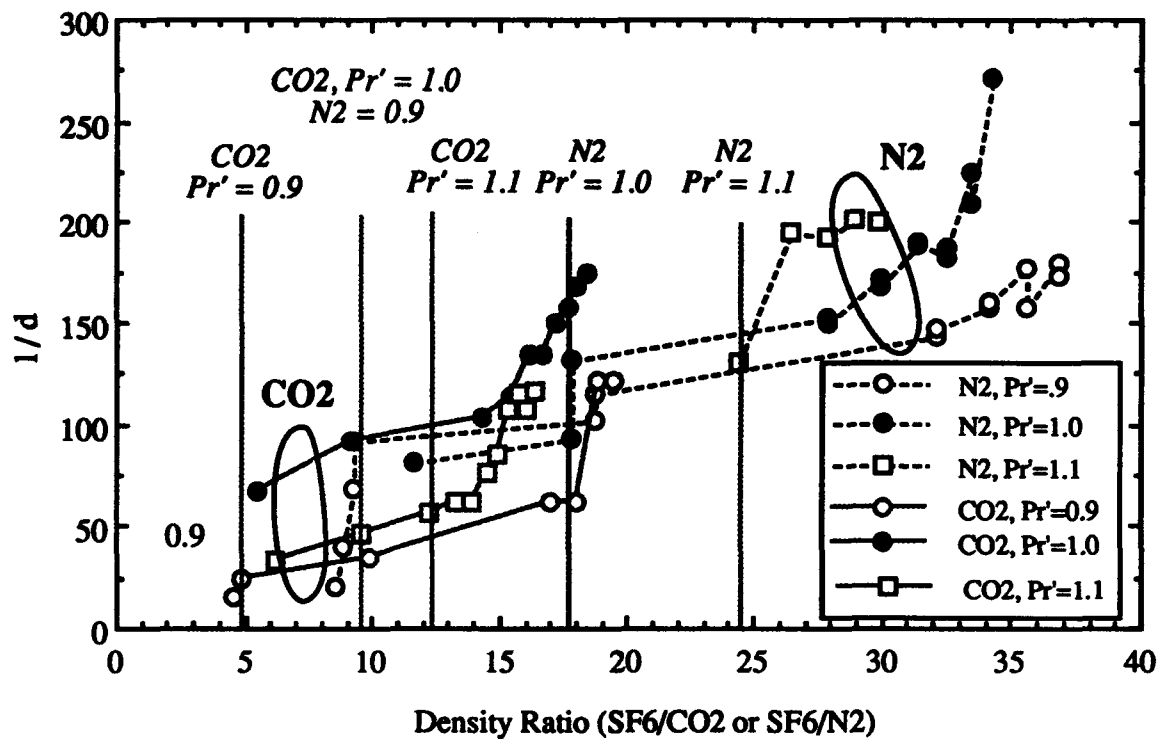


Figure 7. Dimensionless Spray Length Versus Density Ratio

To investigate the effects of density ratio ( $\gamma$ ) on spray penetration, data are plotted as a function of  $\gamma$  in Fig. 7. The critical temperature conditions are also marked in the figure for the three chamber pressures examined. The spray length decreases with decreasing density ratio. For the N<sub>2</sub> environment, a sharp decrease is observed at  $\gamma \approx 25, 18$ , and  $9$ , or the critical temperature state ( $Tr = 1.0$ ) for  $Pr = 1.1, 1.0, 0.9$ , respectively. This correlation with the critical temperature, however, is not observed for the CO<sub>2</sub> environment.

The mixture pseudo-critical pressures and temperatures are plotted as a function of mixture fraction,  $f$ , in Figs. 8 and 9, respectively. The mixture fraction is defined as the mass fraction of injected fluid, SF<sub>6</sub>, in the flow field with  $f = 0$  denoting the ambient fluid and  $f = 1$  the injected fluid. Also plotted in Fig. 9 are the mixture temperatures. An adiabatic mixing between SF<sub>6</sub> and ambient fluid is assumed with ambient fluid at 290 K and SF<sub>6</sub> at  $Tr = .92, .94, .96, .98, 1.00$ , or  $1.02$ . The temperature is obtained based on the Lee-Kesler equation of state and the pseudo-critical properties. From a single component point of view, the mixture will be at a supercritical state when  $T > Tr$  and  $P > Pr$ . The pseudo-critical pressure of the SF<sub>6</sub>/N<sub>2</sub> mixture is lower than the SF<sub>6</sub> critical pressure (or chamber pressure) over the region  $f < 0.6$  and higher over  $0.6 \leq f < 1$ . For SF<sub>6</sub>/N<sub>2</sub>, the mixture temperature is generally above the mixture critical temperature, except for  $f > 0.92$  when the injector fluid is at  $Tr < 1.00$ . Thus, SF<sub>6</sub>/N<sub>2</sub> will be generally in the supercritical regime for  $f < 0.6$  and in the subcritical regime for  $0.6 \leq f < 1.0$  (except for  $Tr < 1$  and  $f > 0.92$ ). The pseudo-critical pressure of the SF<sub>6</sub>/CO<sub>2</sub> mixture is higher than the chamber pressure for the entire mixture fraction space (i.e., all the mixing states). Therefore, SF<sub>6</sub>/CO<sub>2</sub> will be in the subcritical regime through out the mixing. It is also worth noting that the SF<sub>6</sub>/CO<sub>2</sub> mixture temperature is generally lower than the pseudo-critical temperature, except for mixture fractions near unity when the injector fluid is at  $Tr > 1$  (i.e., for  $f > 0.94$  with injector fluid at  $Tr = 1.02$  among the six injector temperatures examined).

The mixture pseudo-critical property calculation suggests that the subcritical state exists in SF<sub>6</sub>/N<sub>2</sub> sprays over the mixture fraction bounded by  $0.6 \leq f < 1$  and exists in SF<sub>6</sub>/CO<sub>2</sub> sprays over the entirely mixture fraction space except for the small regime near  $f = 1$  as noted earlier. The

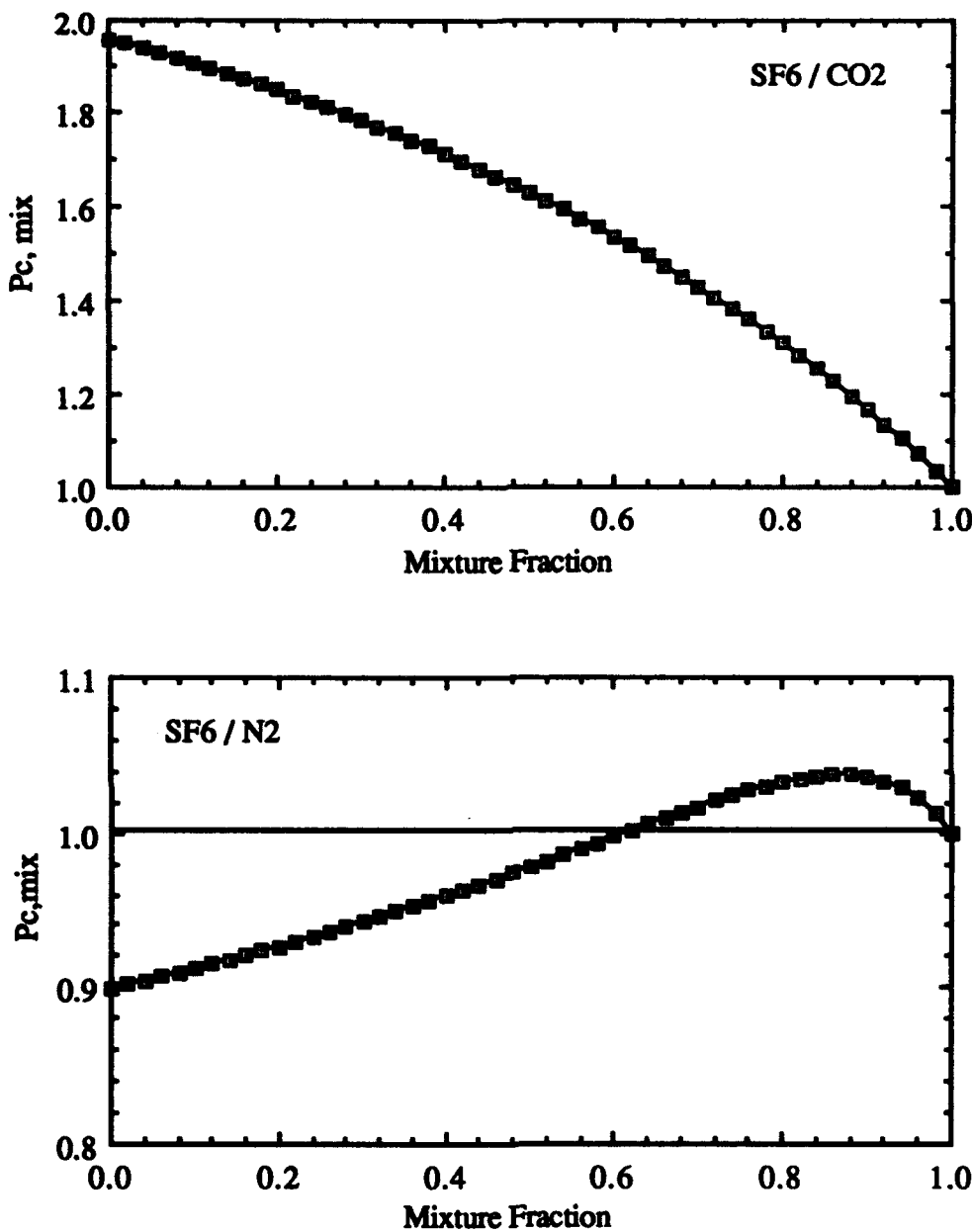


Figure 8. Calculated Mixture Pseudo-Critical Pressures as a Function of Mixture Fraction.

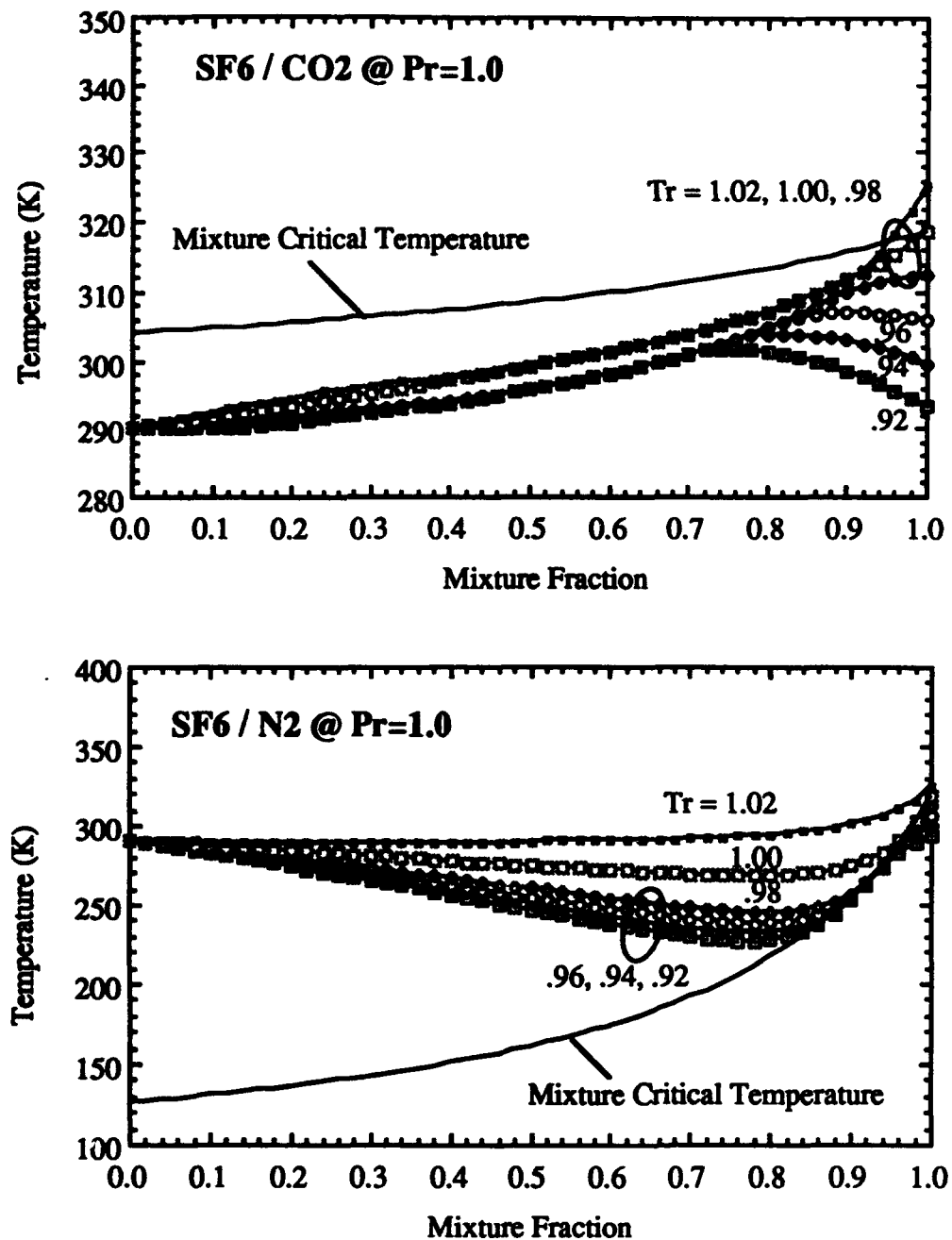


Figure 9. Calculated Mixture Pseudo-Critical Temperatures as a Function of Mixture Fraction.

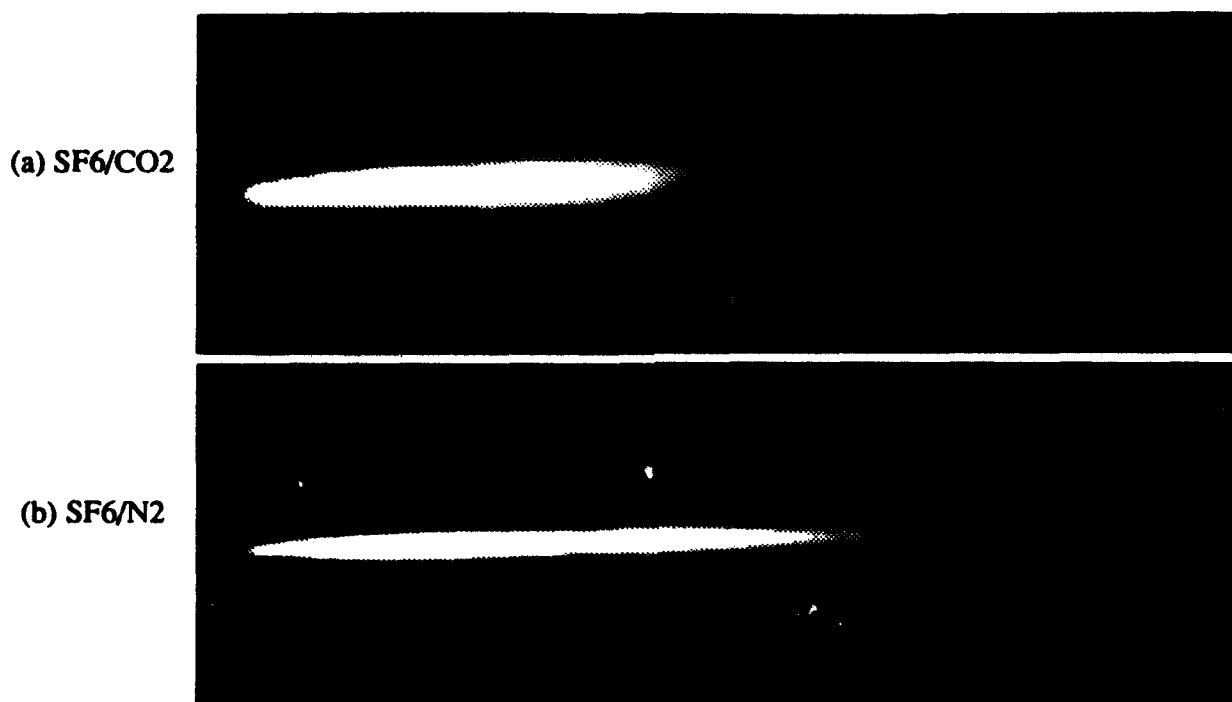


Figure 10. Averaged images of  $\text{SF}_6/\text{CO}_2$  and  $\text{SF}_6/\text{N}_2$  spray at  $\text{Tr} = 0.95$  and  $\text{Pr} = 1.0$

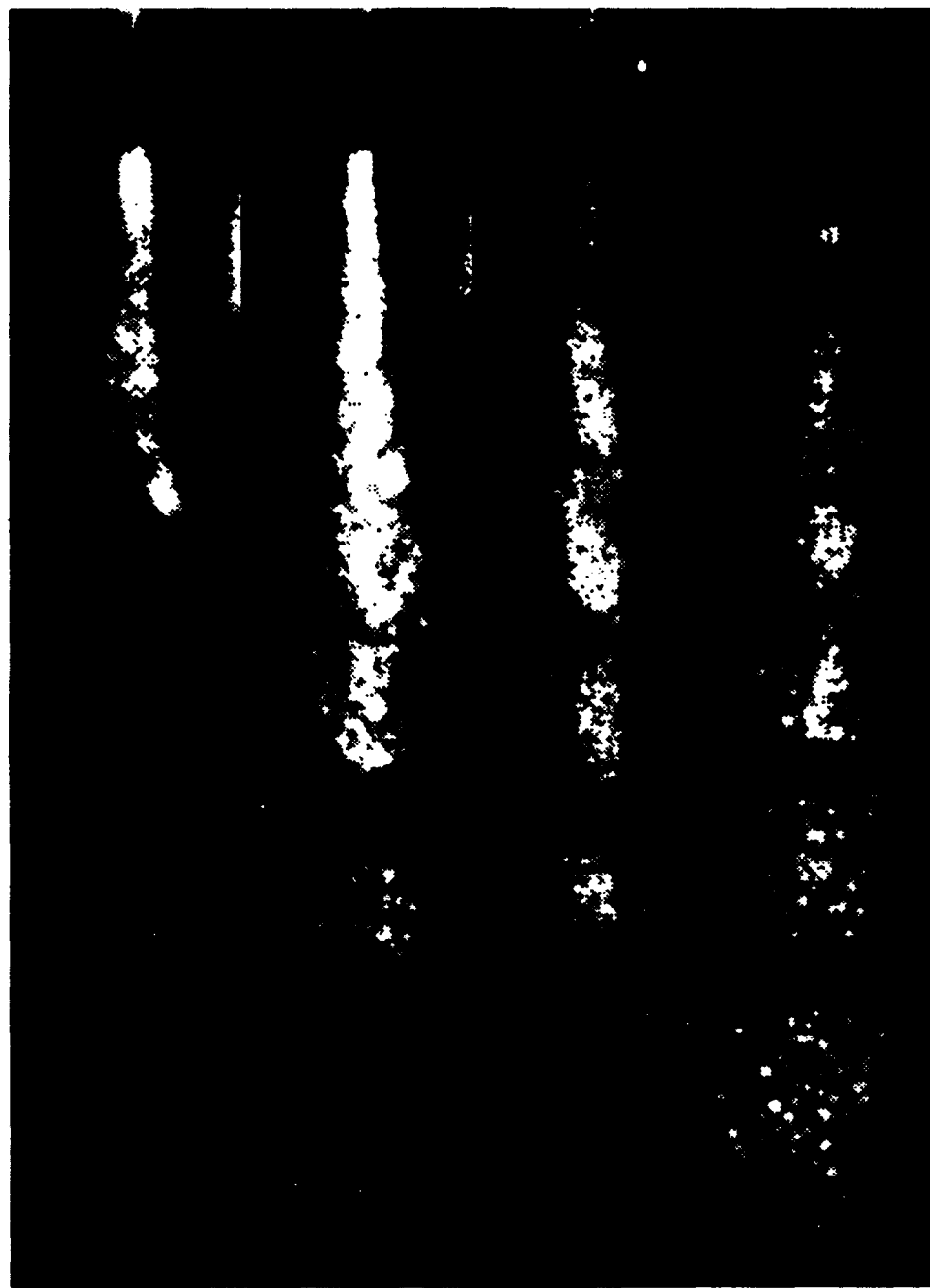
**SF<sub>6</sub> / CO<sub>2</sub>**

Tr=1.01

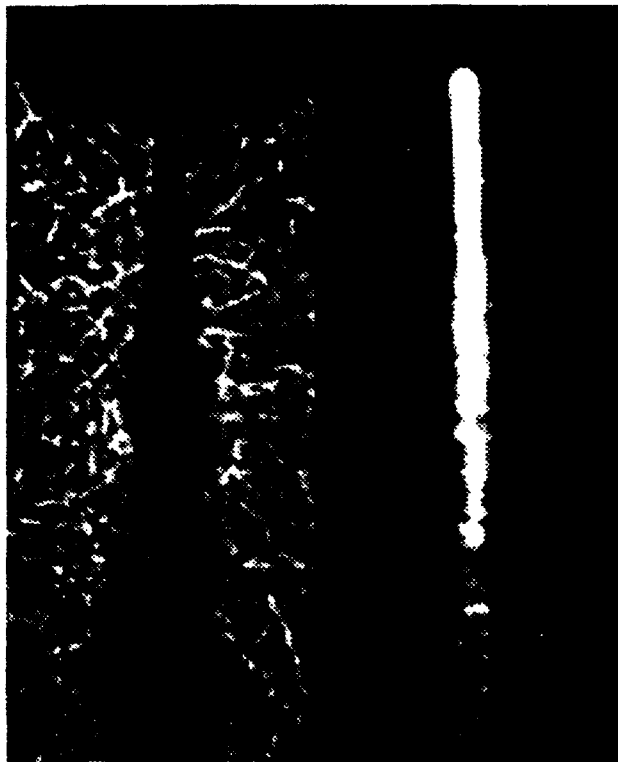
Tr=1.00

Tr=0.99

Tr=0.93



**Figure 11.** Instantaneous images of SF<sub>6</sub>/CO<sub>2</sub> sprays at Pr = 1.0

**SF<sub>6</sub> Injection into N<sub>2</sub> @ Pr= 1.0****Shadowgraph  
Tr=0.94****Sheet-lighting  
Tr=0.94****Shadowgraph  
Tr=1.00****Sheet-lighting  
Tr=1.00****Figure 12. Instantaneous Image of SF<sub>6</sub>/N<sub>2</sub> Sprays at Pr = 1.0.**

calculation therefore suggests that the SF<sub>6</sub>/CO<sub>2</sub> spray has a wider spray angle and a longer spray length under a comparable injector condition. The wider spray angle and longer spray length indeed can be seen from the averaged light scattering image shown in Fig. 10. When the spray length is plotted as a function of density ratio as shown by Fig. 7, the CO<sub>2</sub> environment with Pr' = 1.0 (i.e., with the chamber being maintained at SF<sub>6</sub> critical pressure) has a longer spray length over 12 < γ < 18. The CO<sub>2</sub> environment, however, has a shorter spray length for Pr' = 0.9 over 10 < γ < 18, in contrary to the prediction of pseudo-critical mixture states. Only when the injected fluid density decreases below the critical-sate value (i.e., γ below 9 for Pr' = 0.9) the N<sub>2</sub> environment has a shorter spray length. At this density ratio (or rather when the injector fluid temperature reaches the critical temperature), the spray length decreases sharply. A similar sharp-decrease is also seen for the N<sub>2</sub> environment at Pr' = 1, e.g., at γ ≈ 18 in Fig. 7. As for CO<sub>2</sub> environment, such sharp decrease is less obvious. It appears that the injection of near- or super-critical SF<sub>6</sub> into N<sub>2</sub> environment results in a flashing-like atomization while the CO<sub>2</sub> environment does not.

The instantaneous light scattering images of the SF<sub>6</sub> sprays in CO<sub>2</sub> environment are shown in Figure 11 for injector fluid at Tr = 0.93, 0.99, 1.00 or 1.02. The calculation of mixture pseudo-critical states of SF<sub>6</sub>/CO<sub>2</sub> sprays suggests that the mixture fraction is typically subcritical. The spray imaging of Fig. 11 shows jet-like mixing or structures for the CO<sub>2</sub>/SF<sub>6</sub> sprays. The jet-like structures are shown by the "fine mists" formed in the flow, in which large vortical structures can also be identified. When the injector temperature increases, the "mist" region is reduced which is evident from the comparison of the images taken at Tr = 0.93 and 1.02. The formation of mist-like droplets in the flow could result from the local equilibrium and it in turn yields subcritical state-drops. It appears that the mixing process, instead of the break-up of a liquid core, dictates the formation and the "spread" of the droplets. When the injector temperature is increased, the injected fluid although initially being supercritical, the mixture is sub-critical. Therefore, droplets will form when the mixing between the injector and ambient fluids occurs. Far away from the injector, e.g., f = 0, the ambient fluid exists in vapor phase. Moving toward the jet core (or f > 0), the liquid

phase (or formation of droplets) will appear when the local SF<sub>6</sub> vapor pressure (or fugacity) assumes the value determined by the phase equilibrium and mixing considerations. When the injector temperature (or the excess enthalpy) increases, the spray behaves like a flashing atomization of superheated liquids. When the temperature or the superheat increases, the available excess enthalpy for vaporization increases and the volume occupied by the liquid phase decreases.

As for the injection of SF<sub>6</sub> into N<sub>2</sub> environment, the mixture fraction is supercritical for  $f < 0.6$  and strong flashing-like atomization is likely to exist when the injector fluid is maintained at a near or supercritical temperature (cf. Figs. 8 and 9). The instantaneous imaging of SF<sub>6</sub>/N<sub>2</sub> sprays shows (Fig. 12) that the liquid phase (or a stronger scatter) exists only in the core of the jet. The mist-like droplets are not obvious in the ICCD image of Fig. 12; however, the jet boundary extends far beyond the dense core as evident from the shadowgraph images. The absence of mist-like droplets is probably due to the fact that the mists or droplets are indeed not formed or the intensity of scattered light is below the detection limit set for the particular visualization. When the injector temperature is increased from  $Tr = 0.94$  to 1.00, the volume of the dense core decreases (shown by light scattering images) and the vapor core remains qualitatively similar.

#### 4.3 Uncertainty Estimates

The sensitivity in the measurements of the spray length due to the threshold value is summarized in Fig. 13. The relative error is defined as the length for pixel intensity below a threshold value divided by the measured length. The threshold length is determined by a cubic polynomial curve fit of the axial profile and the threshold pixel value is chosen to be 5 (the full scale value is 255). Most errors are within 5% of the measured length. The error becomes larger when the spray length is short due to strong flashing-like atomization, e.g., SF<sub>6</sub>/CO<sub>2</sub> at  $Pr = 0.9$ , or when the dense fluid is confined in the core region and the break-up of fluid parcels is recorded, e.g. SF<sub>6</sub>/N<sub>2</sub>.

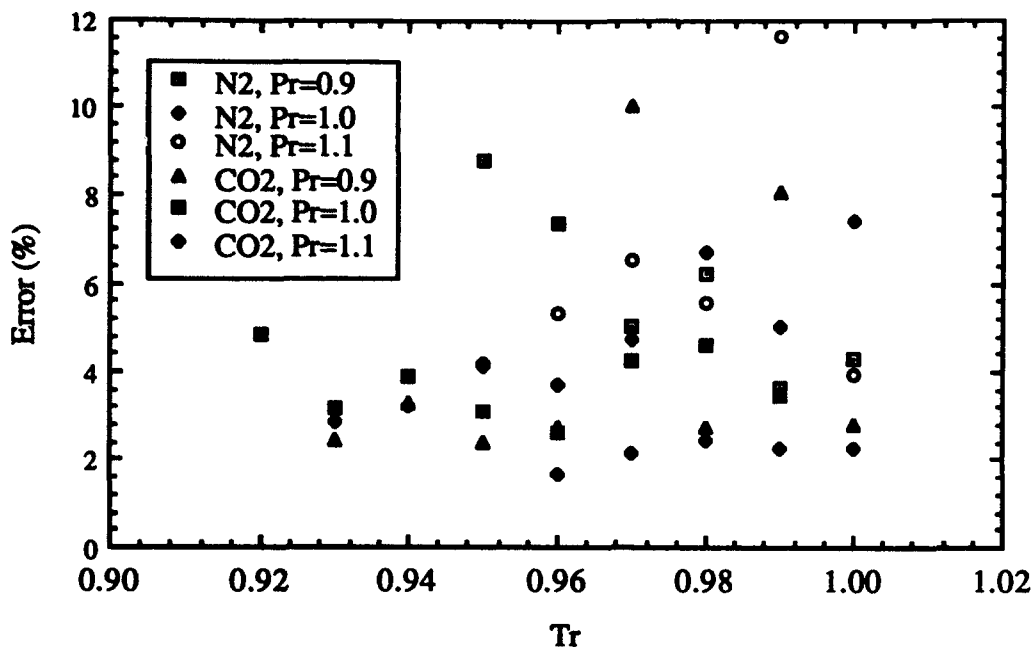


Figure 13. Error Estimate for the Spray Length Measurements.

#### 4.4 Summary

The spray length measurement, the calculation of mixture pseudo-critical temperatures and pressures, and the instantaneous light scattering and shadowgraph images provide new insight into the injection of supercritical fluids into an environment of dissimilar fluids. A simulant fluid, SF<sub>6</sub>, and two environments, N<sub>2</sub> and CO<sub>2</sub>, are examined. Mist-like droplets with characteristics of jet mixing are typical for the CO<sub>2</sub> environment, consistent with the mixture critical state calculation which shows that the respective mixture fraction space is subcritical. Narrow and dense cores are typical in the light scattering imaging of SF<sub>6</sub> in N<sub>2</sub> environment with the shadowgraph showing a jet-like spread, consistent with the mixture critical state calculation showing that the mixture fraction space is subcritical primarily for the region  $0.6 \leq f < 1$ . The mixing of dense fluids appears to dictate the spread of the mist-like droplets in CO<sub>2</sub> environment and the spread of the vapor in N<sub>2</sub> environment. The flashing-like atomization is another characteristics in the sprays reported in the present investigation. The present results call for further investigation on the mixing characteristics of supercritical sprays.

## VII. REFERENCES

- Chen, L.-D., Sui, P.C., and Roquemore, W.M., 1993, "Dynamic Characteristics of a Buoyant Jet Diffusion Flame," *Bulletin of the American Physical Society*, Vol. 38, No. 10.
- Hsu, K.-Y., Chen, L.-D., Katta, V. R., Goss, L. P., and Roquemore, W. M., 1993a, "Flame-Vortex Interactions in a Driven Diffusion Flame," *APS Physics of Fluids A. Fluid Dynamics* (in Gallery of Fluid Motion), Vol. 30, p. S4.
- Hsu, K. Y., Chen, L.-D., Katta, V.R., Goss, L.P., and Roquemore, W. M., 1993b, "Experimental and Numerical Investigations of the Vortex-Flame Interactions in a Driven Jet Diffusion Flame," AIAA Paper 93-0455, Thirty-first Aerospace Science Meeting held in Reno, Nevada, 11-14 January, 1993.
- Lee, S., 1992, "Flow-Flame Interaction of Nitrogen-Diluted Hydrogen Jet Diffusion Flame," Ph.D. Dissertation, Department of Mechanical Engineering, The University of Iowa, Iowa City, Iowa, December 1992
- Lee, S., Chen, L.-D. and Roquemore, W. M., 1994, "Vortex Crossing Frequency in a Transitional Jet Diffusion Flame," *25th International Symposium on Combustion, The Combustion Institute* (in review).
- Lin, H.-W., 1993, "Numerical Simulation of the Dynamics and Instability of Flame Flicker when Subject to Perturbed Boundary Conditions," Ph.D. Dissertation, Department of Mechanical Engineering, The University of Iowa, Iowa City, Iowa, December 1993.
- Reid, R. C., Prausnitz, J. M., and Poling, B. E., 1987, *Properties of Liquids and Gases* (4th Ed.), McGraw Hill.
- Reitz, R. D. and Bracco, F. V., 1986, "Mechanisms of Breakup of Round Liquid Jets," in *Encyclopedia of Fluid Mechanics, Vol. 3, Gas-Liquid Flows* (N. P. Cheremisinoff, Ed.), Gulf, pp. 233-249.
- Roquemore, W. M., 1992, Private Communication (pressure chamber designed by G. W. Switzer at Wright Laboratory).
- Switzer, G. W., 1992, Private Communication
- Szetela, E. J., and TeVelde, J. A., 1982, "Experimental Study of External Fuel Vaporization," SAME Paper No. 82-GT-59.
- Williams, F. A., 1985, *Combustion Theory* (2nd Ed), Benjamin/Cummings.

**APPENDIX A**

**VORTEX-FLAME INTERACTION**



AIAA 93-0455

**Experimental and Numerical Investigations of  
the Vortex-Flame Interactions in a Driven Jet  
Diffusion Flame**

K. Y. Hsu and L. D. Chen  
Department of Mechanical Engineering  
The University of Iowa  
Iowa City, IA

V. R. Katta and L. P. Goss  
System Research Laboratories, Inc.  
Dayton, OH

W. M. Roquemore  
Wright Laboratory  
Wright-Patterson Air Force Base, OH

**31st Aerospace Sciences  
Meeting & Exhibit**  
**January 11-14, 1993 / Reno, NV**

## EXPERIMENTAL AND NUMERICAL INVESTIGATIONS OF THE VORTEX-FLAME INTERACTIONS IN A DRIVEN JET DIFFUSION FLAME

K. Y. Hsu and L. D. Chen\*  
Department of Mechanical Engineering  
The University of Iowa  
Iowa City, IA 52242

V. R. Katta\*\* and L. P. Goss\*\*  
System Research Laboratories, Inc.  
Dayton, OH 45440-3696

W. M. Roquemore†  
Wright Laboratory  
Wright-Patterson Air Force Base, OH 45433

### Abstract

This paper presents the initial results of a vortex-flame interaction that is periodically reproduced. The interaction has features that are similar to those observed in a turbulent jet diffusion flame. An acoustic speaker is used to form axisymmetric, counter rotating ring vortices inside the flame surface. Phase-locked Reactive-Mie-Scattering (RMS) and Planar-Laser-Induced-Fluorescence (PLIF) are used to visualize the vortex structure and OH zone, respectively. The evolution of the vortex-flame interaction is presented. The forcing vortex, convected in the radial direction, causes the flame to bulge outward. When the flame surface is further stretched, a local quenching around the flame is observed. Thin-Filament-Pyrometry (TFP) is used to record the temperature variation during the interaction process. A sudden decrease in flame temperature indicates the occurrence of local quenching. The thinning and disappearance of the OH zone during the quenching process is also illustrated by OH-PLIF imaging. A time-dependent numerical simulation reproduces the vortex structure and the dynamic vortex-flame interaction observed in the experiment. Although the fast chemistry model fail to predict the quenching, the calculation demonstrates the importance of transport phenomena during the vortex-flame interaction.

### Introduction

Lean blowout, high altitude relight, emissions, and combustion efficiency are of practical importance

in the design of gas turbine combustors. They all involve turbulent combustion processes that need to be better understood if accurate combustor design models are to be developed. Turbulent jet diffusion flames are used to gain insight into turbulent combustion processes and to develop numerical models for use in combustor design. Because of their practical importance, they have been studied for over 40 years. Although considerable progress has been made in understanding turbulent jet diffusion flames, there still remain many important questions about the turbulent combustion processes and the simplifying assumptions required to effectively model them. The conceptual view of turbulent reaction zones and the interplay between turbulence and chemistry are germane to the modeling approaches. Recent research has focused on whether turbulent flames can be viewed as an ensemble of strained laminar flamelets or distributed reaction zones (Bilger, 1989; Correa, 1992). In this paper the statistical fabric of a turbulent reaction zone is viewed as an ensemble of vortex-flame interactions. The statistics of the problem are eliminated by isolating and studying a single vortex-flame interaction event that has similar characteristics to those occurring in turbulent jet diffusion flames.

Many of the basic characteristics of turbulent jet diffusion flames were described by Hottel and Hawthorne (1949), Scholefield and Garside (1949), and Wohl et al. (1949). According to their description, a vertically-mounted jet diffusion flame is considered fully turbulent when its entire surface area becomes a flame brush, which means that the flame has a highly wrinkled, bumpy, or rough appearance.

Improved visualization techniques have provided additional insights into the structure of a turbulent flame and the events that happen as the flame becomes turbulent (Roquemore, et al., 1988). Although the turbulent transition processes can be

\* Professor, Member

\*\* Research and Application Division, Member

† Fuel and Lubrication Division, Member

This paper is declared a work of the U.S. Government and is not subject to copyright protection in the United States

observed in flames established with fuel tubes (Takeno and Kotani, 1977; Takahashi, et al. 1982), they are more clearly observed when the jet flame is established by a contoured nozzle with a flat velocity exit profile (Yule et al. 1981; Eickhoff, 1982; Savas and Gollahalli, 1986; Coats and Zhao 1988; and Roquemore et al. 1988). At transitional jet velocities, well organized, axisymmetric vortex structures are observed to exist inside the laminar flame surface for many jet diameters downstream. As the jet velocity increases, the inner vortices begin to coalesce at a downstream location in the flame. The coalescence process is highly unstable and results in the break-down of the organized vortices into smaller but identifiable three dimensional fluid elements. The flame becomes turbulent when these small three-dimensional structures interact with the flame creating the turbulent flame brush. The height at which this takes place is called the break-point. As the jet velocity increases, the break-point moves toward the nozzle exit. When the break-point is occurred near the lip of the nozzle, the flame is considered to be fully turbulent. Thus, the wrinkles or bumps in the flame are localized protrusions of the flame surface that result when three-dimensional fluid elements of different size, shape, velocity, and rotational strength interact with reaction zones of different thicknesses.

There is a question about whether or not the small three-dimensional fluid elements formed in the coalescence process are vortices. In a vortex, the fluid mass moves around a common axis (Lugt, 1979). Some of the small structures in turbulent jet flames are easily recognized in a two-dimensional visualizations as vortex pairs that are associated with mushroom-shaped vortices. Other fluid elements are not so easily recognized as vortices in the laboratory reference frame. However, three-dimensional calculations show that the small fluid elements resulted from the coalescence of two-dimensional vortices are vortex structures (Knio and Ghoniem, 1989). Since this process is similar to that occurring in jet flames, it will be assumed that the three-dimensional fluid elements that interact with the flame are vortices. The interaction processes will be referred to as vortex-flame interactions.

Individual vortex-flame interactions are important to understand for several reasons. First, they can increase or decrease the turbulent reaction rate. When the vortex-flame interactions is moderate, they increase the surface area of the flame which leads to an overall increase in the global reaction rate and a reduction in the length of the flame. However, if a vortex has a sufficiently high radial velocity, it can pass through the flame creating a localized hole in

which no chemical reactions take place (Takahashi and Schmoll, 1990; Chen and Goss, 1991; Takahashi and Goss, 1992). The holes can cause the flame to split or lift when they form near the jet exit. If the holes covers two much of the flame surface the global reaction rate can decrease. This can lead to reduction in combustion efficiency and blow-out. Second, flame vortex interactions may be building blocks for statistical theories of turbulent flames. It is conceivable that an ensemble of only a relatively few basic types of vortex-flame interactions need to be considered to accurately represent the statistical result of what, on first sight, might appear to be an endless number of interactions. If this idea is supported by experimental results, it might be feasible to construct a statistical turbulent combustion model.

Vortex-flame interactions have been studied experimentally as well as computationally. However, most of the studies are for premixed systems (Roberts et al., 1992; Rutland and Ferziger, 1989; Poinsot et al., 1991). The studies of diffusion flames appear to involve vortex-flame interactions that apply to the flame interacting with the large buoyancy induced vortex structures formed outside transitional jet flames (Karagozian and Marble 1986; Laverdant and Candel 1989). In turbulent jet diffusion flames surrounded by nearly still air, the vortices must be transported from the fuel side of the flame towards the diffusion flame surface. To our knowledge, only one individual vortex-flame interaction study has been performed under these conditions and it was complicated by the coupling of a large, buoyancy induced, vortex that was outside of the flame surface with the vortex inside the flame surface (Lewis, 1988).

This paper presents the initial results of a vortex-flame interaction that has some features like those observed in turbulent jet diffusion flames. A counter rotating pair of ring vortices are formed by driving the flow. Planar visualization and line-temperature measurement techniques are phase-locked to the driving pulse so that the interaction can be strobe at different time steps. A direct numerical simulation with infinitely fast chemistry, unity Lewis number, and temperature and concentration dependent transport coefficients (Katta et al., 1992) is used to investigate the dynamic characteristics of the vortex-flame interaction.

### **Experimental Descriptions**

The vortex-flame interactions are produced in an externally driven methane jet diffusion flame shown schematically in Fig. 1. This is a very flexible

system that allows the frequency, intensity, and shape of the driving pulse to be varied. A speaker connected to a 25 mm diameter fuel tube is used to periodically generate the vortices. The speaker is placed inside a chamber with the speaker diaphragm oriented vertically upward along the flow direction. The chamber is sealed from the surrounding air. The fuel enters the speaker chamber through side inlet ports. Another fuel inlet, at a location just above the chamber, is used for seeding in visualization. A power amplifier in conjunction with a pulse generator are used to drive the speaker, which forces the fuel through the fuel tube. Vortices are formed inside the flame near the tip of a 10 mm diameter long-tapered nozzle. The strength and the frequency of the generated vortices can be adjusted by the pulse generator. The flame is shielded from room air disturbances by a slowly co-flowing annulus air. The air duct (152 mm diameter) consist of diffusion and contraction sections and layers of screens and honeycombs for flow straightening so the surrounding air flow is relative quite. The vortex-flame interaction is studied using visualization, velocity and temperature measurement techniques that are phased-locked to the driving pulse.

#### Reactive-Mie-Scattering Imaging

The detailed structures of the driven vortices and the flame are visualized using a Reactive-Mie-Scattering (RMS) technique (Chen and Roquemore, 1986). The output beam (532 nm) of a pulsed Nd:YAG laser is used to form a laser sheet (1 mm thickness) vertically along the center-line of the jet flame as shown in Fig. 1. The vortical structures are visualized by the scattering of micron-size TiO<sub>2</sub> particles formed from the chemical reaction between the TiCl<sub>4</sub> vapor seeded in the fuel and the combustion product, H<sub>2</sub>O. A 35 mm camera placed at a right angle to the laser sheet is used to photograph the vortical structure and the flame. A gated mechanical shutter mounted on the camera is triggered externally. In order to visualize the detailed dynamics of the flame-vortex interaction, a synchronization circuit is used to trigger the Nd:YAG laser, speaker, and camera shutter. A master pulse generator in combination with a delay circuit is used to create an adjustable time delay between the speaker and the Nd:YAG laser for phase-locked visualization.

#### Joint RMS-PLIF Imaging

The vortex structure and the OH zone are visualized simultaneously using Reactive-Mie-

Scattering (RMS) and Planar-Laser-Induced-Fluorescence (PLIF). The experimental setup of the RMS-PLIF system is shown in Fig. 2. The frequency-doubled laser beam (532 nm) of a pulsed Nd:YAG laser is used to pump a dye laser. The output UV beam (282.7 nm) from the wavelength extender is tuned to excite the OH-radical (Hanson, 1986). A quartz focusing lens and a cylindrical lens are combined to expand the UV laser sheet vertically along the center-line of the flame. A gated intensified-CCD camera is used to record the fluorescent image of the OH-radical at a right angle to the laser sheet. The phase-locked measurement is accomplished by precise synchronization between the laser, speaker pulse, and CCD camera. The intensifier, gated by a pulse generator with 1.5 ms gate width, is used to eliminate the flame background emission. The Mie scattering of the TiO<sub>2</sub> particle marks the region where the fuel and products, H<sub>2</sub>O, are mixed.

#### Laser-Doppler-Anemometry

A frequency-shifted Laser-Doppler-Anemometry (LDA) system is used for velocity measurement. The fuel is seeded with Al<sub>2</sub>O<sub>3</sub> particles (5  $\mu\text{m}$  mean diameter). The time history of the velocity is measured by employing a phase-locked, conditional sampling method. A 5 ms time window is used to register 1000 samples at each phase angle.

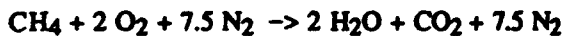
#### Thin-Filament Pyrometry

The line temperature is measured by Thin-Filament Pyrometry (TFP) technique (Vilimpo and Goss, 1988) as shown schematically in Fig. 3. A fine SiC fiber with approximately 15  $\mu\text{m}$  diameter is supported and placed horizontally across the center of the flame. The thermal radiation from the heated filament is focused onto a ten-facets spinning mirror. An InGaAs detector with spectral range of 900 to 1500 nm is used to measure the radiative signal from the filament. The emission intensity along the filament is scanned continuously onto the detector by the spinning mirror. A 12-bit waveform recorder is used to digitize and store filament intensity. A He-Ne laser and a photodiode are used as the triggering signal for initiating data acquisition. The line intensity of the filament is scanned on to the InGaAs detector at a 2 kHz frequency. The InGaAs detector signal is digitized by the waveform recorder at 5 MHz frequency. A program is used to interface the waveform recorder and a Macintosh IIfx for data

acquisition and transfer. The digitized TPP data consist of 1024 points in spatial direction and 512 segments in temporal direction. The recorded TPP data has spatial and temporal resolutions of 35  $\mu\text{m}$  and 500  $\mu\text{s}$ , respectively. The time trace of the driving pulses is digitized by a multi-channel 16-bit A/D converter. The TPP data is collected at 20 different axial locations above the nozzle exit. The flame background emission is also recorded at those same locations. Background subtraction with precise phase-matching is performed on the TPP data to eliminate the flame emission. The recorded time trace of the driving pulses ensure precise phase-matching in data reduction. Temperature is calculated from the processed TPP data. The detailed calibration and correction of the TPP measurement has been discussed by Vilimpoc and Goos (1988). Phase-averaging on temperature is performed over 7 cycles at each axial location. The phase-averaged temperature profiles calculated at each location are used to reconstruct the two-dimensional temperature field at different phase angles.

#### Numerical Scheme

The diffusion flame considered in this work is formed between a central methane jet and a low speed co-annular air flow. Time dependent governing equations, expressed in cylindrical coordinates, consist of mass continuity, axial and radial momentum conservation, and two scalar conservation equations (Katta et al. 1992). Shvab-Zel'dovich formulation in conjunction with the flame-sheet model is assumed. This formulation is primarily used in understanding the mechanism leading to large vortices that are observed in the experiments and their effects on the flame surface. Body-force term, due to the gravitational field, is included in the axial momentum equation. The following global chemical kinetics between methane and oxygen is considered :



Nitrogen in this system is assumed to be an inert gas. The system of governing equations is completed by using the state equation. Transport properties (viscosity and diffusion coefficient) are considered to vary with temperature and species concentrations. The enthalpy of each species is calculated from polynomial curve-fits, while the viscosity of the individual species is estimated from Chapman-Enskog collision theory. The binary diffusion coefficient between any two species on the fuel side of the flame is assumed to be identically

equal to that of the fuel and nitrogen. Similarly, on the oxidizer side of the flame it is made identical to that of the oxygen and nitrogen. Chapman-Enskog theory and the Lennard-Jones potentials have been used to estimate these two binary diffusion coefficients.

The finite-difference form of the governing equations are constructed on a staggered grid system based on an implicit QUICKEST numerical scheme. It is third-order accurate in both space and time and has a very low numerical diffusion error. At every time-step, the pressure field is accurately calculated by solving the system of algebraic pressure Poisson equations simultaneously, at all grid points by using LU decomposition technique. An orthogonal grid system with rapidly expanding cell sizes in both  $z$  and  $r$  directions is utilized. The outer boundaries of the computational domain are shifted sufficiently far enough to minimize the propagation of disturbances into the region of interest. Outflow boundary in these flows is the most difficult one to treat because the flow leaving this boundary continuously evolves in time as the large vortices convect through this boundary. A simple extrapolation procedure with weighted zero- and first-order terms is used to estimate the flow variables on the boundary in the present calculations. The main criterion used in selecting the weighting functions is that the vortices crossing the outflow boundary should leave smoothly without being distorted.

Calculations, using a mesh size of 151 x 61 have been made for the unsteady flow in a 250 mm x 150 mm computational domain. Flat initial velocity profiles, with the measured mass-averaged values of 1.5 and 0.4 m/s, have been used at the exit planes of a 10 mm-center-nozzle and a 150 mm annulus-duct, respectively. Because of the gravity term in the axial-momentum equation the computed flame developed a low-frequency oscillation of about 20 Hz. However, no roll-up of the buoyancy-induced vortex occurred within an axial distance of 250 mm.

The large driven-vortices in the experiment are then simulated by periodically perturbing the fuel mass-flow-rate at the exit of the fuel-nozzle at a frequency of 30 Hz. The modified velocity at this section, for a period of one perturbation cycle, is shown in Fig. 4 along with that of the measured one. Note that there is a suction pulse of -1.5 m/s for a period of about 6 ms making the modified velocity zero. This stagnant condition at the nozzle exit pulls the flame surface and thereby, the viscous fluid closer to the axis. The following sudden injection of additional fuel at a velocity of 6 m/s (modified velocity is 7.5 m/s) makes a collision with the highly

viscous combustion products. This process results in sending an axisymmetric, counter rotating pair of ring vortices radially toward the flame surface. The growth and the interaction of this vortex with the flame is further discussed in the results and discussion sections

## Results

The purpose of this study is to investigate vortex-flame interactions that result in flame stretch and extinction processes that are similar to those observed in turbulent jet diffusion flames. With this purpose in mind, but realizing that actual vortex-flame interactions in turbulent combustion processes are three-dimensional and that this seriously complicates both the modeling and experimental efforts, the following characteristics of the vortex-flame interaction were sought. 1) The outward radial velocity of the vortex should be controllable so that vortex-flame interactions results in either the production of a flame bulge, which does not extinguish the flame, or a flame bulge that is stretched to the point that the flame is extinguished, a hole is produced. Similar effects are known to occur in turbulent jet diffusion flames. 2) The interaction should be axisymmetric, since this would facilitate the use of direct numerical simulation and also simplify the experiment. 3) The vortex should interact with a thin, laminar flame so that a flame-sheet model can be used in the simulation. 4) The shape of the vortex was not a major consideration since visualizations have shown that many different shape fluid elements interact with the flame. However, a counter rotating vortex pair are often seen in two-dimensional visualizations of turbulent jets and turbulent jet flames so it would be desirable to produce this type of vortex structure. 5) The vortex-flame interaction should be periodically produced so that phased-locked measurements could be made. This allows the vortex-flame interaction to be studied at discrete time-delays during the interaction process.

A significant investigation was required to determine the driving conditions and the fuel flow rate that would generate a vortex-flame interaction that had the characteristics described above. RMS visualizations were used to systematically investigate the influences of frequency, intensity, and pulse shape on the vortex formation, growth, and flame interaction processes for different air and fuel flow rates. Several problems were encountered. First, it was difficult to find conditions at which a vortex would grow radially to the extent needed to interact with the flame surface. Second, when such conditions were found, the flame would usually lift,

hence the interaction process would not be periodic. Third, the flame would go three-dimensional. Fourth, large buoyancy induced vortices, formed outside the flame, would couple with the inner vortices formed by the driving pulse, so the system would become very complicated. It was found that large internal vortex structures were most evident for flow rates below about 2 m/s and at driving frequencies of 30, 45, 60, and 90 Hz. The calculated resonance frequency of the fuel tube (or the organ pipe effect) was 240 Hz. The frequencies of rapid vortex growth were subharmonics of this frequency, or linear combinations of the subharmonics. However, increasing the amplitude of a sinusoidal wave at a favorable frequency did not produce a desirable vortex-flame interaction for the reasons stated above. The key parameter that lead to the desired vortex-flame interaction was the shape of the driving pulse.

A suitable vortex-flame interaction is produced when the fuel flow rate is maintained at a mean mass velocity of 1.59 m/s and an annulus air velocity of 0.39 m/s. Without driving, the flame is laminar up to a height of 50 mm above the nozzle tip. When a fast rising pulse, with a 12 ms exponential decay, is applied to the speaker at a rate of 30 Hz, a counter-rotating vortex ring is observed to produce a bulge in the blue flame surface. Increasing the intensity of the driving pulse causes a visible hole to form in the stretched flame at a height of 20 mm above the nozzle. The vortex-flame interaction is axisymmetric, periodic, and very repeatable. The dynamics of vortex-flame interaction can be observed with 0.5 ms resolution of the time delay.

The sharp rise, 12 ms decay driving pulse to the speaker results in the axial velocity pulse shown in Fig. 4. The Phase-locked velocity measurements were made on the nozzle centerline, at  $z = 4$  mm. A thousand velocity realizations were averaged at each 1 ms time delay. Data were collected at 33 time-delays which corresponds to one period of the 30 Hz driving frequency. The time-delay was measured from the leading edge of the driving pulse to the middle of the LDA data sampling window. The sampling window had to be opened to 5 ms to obtain a reasonable sampling rate. This means that the measurements at each time-delay were actually averaged over two and a half time-delays on each side of the recorded time-delay. This resulted in the large uncertainties noted by the error bars on the velocity data.

It is seen from Fig. 4 that the mean axial velocity increased from 1.5 m/s and reached a peak of 7 m/s in about 8 ms. This was followed by a gradual decay to 1.5 m/s over a period of 22 ms. There appears to be three inflection points in the decay part

of the velocity pulse. They are located at  $t = 16, 22$  and  $28$  ms. These inflection points are probably due to the mechanical damping of the speaker.

Phase-Locked RMS visualizations at  $8, 10, 12$  and  $14$  ms time-delays are shown from left to right in Fig. 5(a). The vortex structures captured by the RMS visualizations can be recognized by their dark green-yellow appearance. These images are frozen by the  $10$  ns flash of the laser sheet passing through the center of the flame and thus, accurately represent the time and spatial evolution of the vortices. This is not necessarily the case for the images of the flame.

The apparent flame locations in Fig. 5(a) are marked by the yellow and blue colors in the photograph. The yellow color is from the blackbody radiation of the soot particles and the blue is the emissions from the CH radicals in reaction zone of the flame. Both the yellow and blue flames are three-dimensional structures that are superimposed on to a two-dimensional photograph. However, at the outer radial location of the flame, they can be a reasonable two-dimensional representations of the flame surface. Unfortunately the camera shutter had to be opened for  $5$  ms to capture enough light to see the blue flame. This means that the flame images are not truly reflecting the flame "location" at the reported time-delay. This is evident from the image of the blue flame in the  $8$  ms time-delay case. For example, there is an apparent hole in the blue flame that is located above the vortex. This is a false image and only reflects the fact that, during the  $5$  ms shutter opening, centered about the  $8$  ms time-delay, the blue flame spent most of the time at the location where the hole was formed. However, at the higher time-delays, the location of the blue flame doesn't appear to change much, which indicates that the actual changes in the location of the blue flame during the shutter opening are reasonably correct.

The vortex-flame interaction are evident in Fig. 5(a). At the  $8$  ms time-delay, a large vortex that rotates downward is observed. There is also a counter rotating "secondary" vortex on top of the large "primary" vortex but it is to small to be clearly observed. Two milliseconds later, however, the "secondary" vortex is as large as the "primary" vortex. It is clear that they form a pair of counter rotating vortex rings. Almost all of the outward radial motion of the vortices occurs between  $0$  and  $10$  ms. This corresponds to the time that the axial velocity reaches its peak, as noted in Fig. 4. The vortex interaction with the flame produces a hole that occurs between  $8$  and  $10$  ms. This is confirmed by the OH images in Fig. 9. It is also confirmed in Fig. 9 that the vortex never extends radially beyond the flame surface. This

indicates that flame stretch is involved in the flame quenching process. Once the hole is formed and vortex has reached its maximum radial location. The vortex pair then appear to rotate inward as can be observed for time-delays of  $12$  and  $14$  ms. The hole, which is clearly a ring, as noted by the dark band across the flame, remains open for a long time.

The relative axial velocities of the fuel at different radial locations are reflected by the line connecting the vortices on the right and left sides of the flame in Fig. 5(a). The center of the connecting line probably represents a stagnation point as observed by Lewis et al. (1988). At the  $8$  ms time-delay, the vortex connecting line is curved upward, indicating that the vortices, at their outer radial location, have a higher axial velocity than the fluid at the center of the jet. At  $10$  ms, the axial velocities, at the height of the vortices, are nearly independent of radial location. For the  $12$  and  $14$  ms time-delays, the central region of the flow is moving much faster than the outer radial region where the vortices are located. Indeed, the stagnation point moves upward about  $10$  mm between  $10$  and  $12$  ms time delays. This give a velocity of  $5$  m/s, which is in agreement with the data in Fig. 4 for the  $11$  ms time-delay. There is very little vertical motion of the vortices at time-delays between  $10$  and  $14$  ms; however, there is a very large acceleration of the central jet fluid above the vortices. This is caused by inward radial motion of the vortices which produces a jetting action of the central fluid. It is anticipated that this will suck air in towards the fuel stream to replace the volume of fluid being accelerated upwards. The accelerating fluid cannot be replaced by the fluid below the vortex pair because its axial velocity is decreasing (See Fig. 4 for time-delays greater than  $10$  ms) by the inward contraction of the vortices.

The numerical simulation at approximately the same time-delays as those of the experiments of Fig. 5(a) are shown in Fig. 5(b). Composite figures of isotherms (left) and color-coded particle trackings (right) are presented for each time-delay. Also shown in the figure are the predicted instantaneous stoichiometric mixture fraction locations, marked by the white dots outside the particle trackings. The numerical simulation reproduces the evolution of the primary vortex of the experiments using the particle tracking technique. The counter-rotating vortex ring is also evident in the simulation. The isotherm representation did not identify the vortex pair that is shown by particle trackings. In fact, the temperature field prediction seems to suggest the existence of a single vortex region. The numerical simulation appears to produce nearly the same time and spatial

evolution of the ring vortex as observed in with the experimental visualizations.

The simulation shows a thinning of the reaction zone and a decrease in the flame temperature as the flame is being stretched by the vortex-flame interaction. This is noted by the temperature contours in Fig. 5(b). The thinning of the flame seems reasonable but, the actual reduction in the stoichiometric flame temperature is not physically correct for a flame sheet model with fast chemistry. This happens because the reaction zone becomes much thinner than the grid spacing. The grids containing the stoichiometric reaction zone also contains an excess of fuel, so the inadequate grid resolution results in a lower flame temperature.

Phase-locked TFP measurements at 10 and 14 ms are shown in Fig. 6. The TFP temperature data are superimposed on their respective RMS images. The results show that the local peak temperatures (at fixed axial heights) are usually situated along the luminous flame, as one would expect for a laminar or near-laminar jet diffusion flame, except for the region where the vortex is located. The phase-averaged temperature profiles show double peaks in the measurements of the second and third filaments above the burner tube at 10 ms time-delay, and in the upper filaments at 14 ms time delay. At 14 ms time-delay, the outer peak temperature at  $z = 18$  mm (fifth filament above the burner) is 850 K at a radial location  $r = 12$  mm. This radial location is where the local quenching of the "blue" flame is visually observed.

The time trace of the filament temperature in Fig. 7, illustrates that the outward movement of the flame, as noted by the location of the peak temperature, is accompanied by a decrease in the hot zone thickness and a reduction in the peak temperature. The peak temperature location is superimposed on the TFP time trace. When a flame bulge is observed, the "flame" temperature decreases to below the detection limit of 800 K. This decrease in "flame" temperature is accompanied by the appearance of a second temperature peak at a radial location closer to the jet center line. This second peak corresponds to the inner peak shown by the TFP data in Fig. 7. The radial locations of the flame (the outer peak) and the inner peak are also shown in Fig. 7 as a function of time delay. As the flame moves outward, the inner peak in Fig. 7 starts to appear. When the flame is quenched by the vortex-flame interaction, the inner peak temperature becomes higher than the outer peak temperature. The time-evolution of the outer and inner peak temperatures are shown in Fig. 8. The duplicate sets of triangles

illustrate the symmetry of the TFP measurements. The outer peak temperature is seen to decrease from 1800 K to 800 K within the first 3 ms during the rapid growth of the flame radius. The local peak temperature gradually recovers the unperturbed flame temperature.

The time response of the filaments is significant in comparison with the temperature time traces of the flame. The time response of the filament, as the temperature is instantaneously dropped from 1750 K to 300 K, is shown in Fig. 8. The flow remains at 300 K for cooling times of 1, 3, and 5 ms. The response to the filament for these cooling times and a gas flow velocity of 1 m/s are also shown in Fig. 8. The calculated filament temperatures decrease from 1800 K to 1360 K, 850 K, and 650 K for 1ms, 3 ms, and 5 ms cooling pulse widths, respectively. A 3.5 ms cooling period is required, to reach the detector cut-off temperature of 800 K. This suggest that the filament is exposed to a low temperature environment as shown by the time trace in Fig. 7. The time response of the filament is currently being investigated for different convective flow conditions (Post and Gord, 1993).

Four OH-PLIF images at  $t = 9, 11, 13$ , and 15 ms are shown in Fig. 9. These LIF images were taken with the intensifier gate width set at 1.5 ms. Also shown on the LIF images are the RMS visualization taken simultaneously. The vortex interaction with the OH zone (or hot zone) is clearly illustrated in Fig. 9. As the "primary" ring vortex evolves and grows in size, the OH becomes contoured. A local thinning of the OH zone is evident in the visualization taken at the 9 ms time-delay. The radial movement (or growth) of the vortex is sufficient to form a flame bulge. Further outward radial movement of the ring vortex results in a decrease in the local OH fluorescence signal below the detection limit. At this point a hole is formed in the flame, as noted in the 11 ms time-delay image. This local "quenching" persists for a few millisecond, as illustrated by the images at  $t = 13$  and 15 ms. A protruding of the ring vortex is also evident at these two time delays.

## Discussion

The vortex-flame interaction of Figs. 4-9 shows local extinction due to the flame stretch as opposed to other types of the vortex-flame interaction, for example, that resulting from penetration of the fast moving vortices through the flame (reaction) zone as in the formation of the flamelets in jet diffusion flames (e.g., see Roquemore

et al., 1988). The length scale of the ring-vortex pair of the present experiments is much larger than that of the flame zone, and the time scale much longer. These characteristics, however, need not always to be the case for turbulent flames in propulsion systems.

The stretching of the flame due to the vortex action appears to lead to local extinction of the hot (or OH) zone. To obtain a better understanding of the transport process that may be critical to the vortex-flame interaction studied, the numerical simulation at a phase angle similar to the 10 ms time delay of the experiment is studied. The results are shown in Fig. 10(a), using a similar composite image format of Fig. 5(b). The radial profiles of temperature and mole fractions at three axial locations,  $z = 18, 28$  and  $40$  mm, are shown in Fig. 10 (b), by the side of the composite image. The phase angle of 10 ms time delay is chosen because it is in the initial stage of the local extinction and the counter-rotating ring vortex is just being formed. Thus, a better understanding can be obtained for the transport processes critical to these phenomena.

On the formation of the counter-rotating ring vortex, the simulation shows a high radial velocity component in the primary ring vortex. The particle trackings clearly show an outward motion of the jet fluid. This outward motion was deflected at the flame location, due to its inability to penetrate the flame zone, perhaps, due to the barrier of the high viscosity at the flame and/or the large density ratio between the entrained fluid and the flame. While the downward deflected fluid is being entrained into the primary ring vortex, the upward moving fluid forms a counter-rotating ring vortex on top of the primary vortex. The particle tracking of the radial motion mimics a "stagnation-like" layer shown by RMS visualization.

On the transport of species and thermal energy, the radial profiles of temperature and species concentration at  $z = 28$  mm, i.e., location inside the vortex, show sharp gradients of these quantities by both sides of the stoichiometric location. These sharp gradients suggest an enhanced transport of reactants (as can be measured by local scalar dissipation rates) into the reaction zone, and enhanced conductive heat loss from the flame zone. When the fast chemistry assumption is employed, the prediction states that all the reactants transported to the reaction zone will be consumed by the chemical reaction, and at the unity Lewis number limit, the increased heat release rate due to enhanced chemical reaction rates will be balanced by the enhanced conductive heat loss as reflected by the sharp temperature gradients. Thus, an adiabatic flame is always present at the predicted stoichiometric location. In reality, however, the

reaction rate can not keep up, without limit, with enhanced transport of the reactants. As a result, local extinction will occur. In fact, the phase-locked data taken at 10 ms time delay (through 15 ms time delay) suggests that local extinction indeed is present. An interesting observation of the predicted temperature profiles is that at  $z = 28$  mm of Fig. 10(b), the species concentration gradient is so sharp that the present numerical grid resolution is not sufficient to capture the instantaneous stoichiometric location.

On the instantaneous temperature profiles, double peaks in temperature are predicted at the axial location where the primary vortex is present, e.g.,  $z = 28$  mm. The prediction shows that the outer peak at this location ( $z = 28$  mm) corresponds to the stoichiometric location; thus, it has a higher temperature than the inner peak. The TFP data of Figs. 6(a), however, show that the maximum temperature appears at the inner peak location rather than the outer peak. The predicted inner peak temperature at  $z = 28$  mm is a result of the convective transport of hot combustion products into the primary vortex. At the fast chemistry limit, the predicted inner peak temperature is 500 K. The TFP data show an inner peak temperature of 1300 K and the outer peak temperature below 800 K. The convective transport of combustion products from an upstream flame location can not explain the much higher inner peak temperature determined by the TFP measurements. Due to local quenching, it is likely that oxygen can be entrained into the vortex core or it can leak through the reaction zone. As a result, partially premixed flames can exist inside the ring vortex, as well as the convoluted stoichiometric surfaces. To verify the aforementioned hypotheses for the temperature double peaks, the experiments call for concentration measurements inside the ring vortex, and to advance our understanding on the type of the vortex-flame interaction studied, the numerical simulation requires to incorporate the finite rate chemistry for study of the reaction zone structures inside the vortex and the extinction phenomenon.

#### Summary and Conclusion

This paper reports the initial results of a joint experimental and numerical study of the vortex-flame interaction in diffusion flame.

The experimental system periodically reproduces an isolated vortex-flame interaction event that provides a unique opportunity for study of a specific type of the vortex-flame interaction, that leads to local quenching of the flame. The time evolution and the dynamics of the vortex-flame

interaction are quantified by phase-locked measurements of the fuel-jet exit velocity and the flow field temperature, along with phase-locked RMS visualization and PLIF OH imaging.

A ring vortex is periodically reproduced by the driving of the fuel jet using a acoustic speaker, starting near the fuel-jet exit location. This vortex grows in size as time evolves and pushes the location of the luminous flame radially outward. A flame bulge is subsequently formed. During the growth of the primary vortex, e.g., vortex entrainment of the fuel jet fluid, and the time-varying mass addition of the driving, a counter-rotating vortex ring (secondary vortex) is formed. This secondary vortex was initially situated on top of the primary vortex. A "solid-body" type of rotation is subsequently observed from RMS visualizations, showing the rotation of the secondary vortex ring around the primary vortex, or vice versa. This "solid-body" rotation is a result of the faster moving primary vortex.

When the flame bulge is formed, the PLIF images shows a local thinning of the OH zone at the maximum radius location. The thinning of the OH zone suggests the flame being stretched due to the interaction of the vortex and the flame. The continued growth of the vortex size, or the flame bulge radius, eventually results in a local disappearance of the OH fluorescence, coincident with where the filament emissive power falls below the detection limit (i.e., 800K). At this condition the TFP data showed double peaks in radial profiles, unlike without artificial driving, the TFP data show a single peak located outside the luminous flame. The double peak temperature profile shows a higher temperature at the inner peak location.

The numerical model assumes an infinitely fast chemical reaction rate, within the context of the flame sheet model. A finite difference scheme (QUICKEST) is used to obtain solutions to the 2-D, time dependent Navier-Stokes equations, coupled with the continuity and mixture fraction equations. The simulation is seen to reproduce the formation of the primary and secondary vortex pair, and the formation of the flame bulge due to the vortex-flame interaction. The axial height of the flame bulge is also adequately reproduced. Due to the infinitely fast chemistry assumption, the local quenching of the flame is not predicted. The simulation nevertheless shows a double peak temperature profile at the axial location where local quenching was experimentally observed. At this location, the gradients of temperature and concentration are much sharper than the single peak profiles. Due to this sharp gradient, the present numerical grid resolution is not sufficient to precisely

locate the stoichiometry. The maximum temperature, on contrary to the TFP data, is located at the outer peak. The predicted inner peak temperature, however, is much lower than that observed in the experiment.

While the simulation shows the enhanced mass transport to the reaction zone and the transport process being important during the vortex and flame interaction, it fails to predict the flame stretch that leads to local extinction. The much higher inner peak temperature of the TFP data suggest that the finite rate chemistry might be important within the vortex, a result of the premixing of fuel-product mixture with the oxygen that leaks through the quenching location or highly stretched the flame. Thus, it is possible to observe distributed reaction zones or convoluted stoichiometric surfaces inside the ring vortex pair.

This joint experimental and numerical investigation presents an experimental system for study the vortex-flame interaction that undergoes a thin flame regime, through a stretched flame regime, to local extinction. The experimental results suggest the possibility of partial premixing inside the ring vortex pair which is yet to be confirmed.

Several improvements of the current capabilities are obvious. The finite rate chemistry must be incorporated in the numerical model to investigate the reaction zone structure inside the vortex ring. Similarly, the experiment call for species concentration measurements of the ring-vortex pair and quantification of the TFP time response to advance our understanding of the type of vortex-flame interaction studied in this paper.

#### Acknowledgement

This work was sponsored by AFOSR Grant No. F49620-92-J-0462. The authors are indebted to Dr. F. Takahashi for his helpful discussion, D.D. Trump, B. Sarka and M. Post for their assistance.

#### References

- Bilger, R. W., "The Structure of Turbulent Nonpremixed Flames," *Twenty-Second (International) Symposium on Combustion*, The Combustion Institute, Pittsburgh, PA, pp. 475-488, 1989.
- Chen, L.-D. and Roquemore, W. M. "Visualization of Jet Flames," *Comb. and Flame*, Vol. 66, pp. 81-86, 1986.
- Chen, T. H. and Goss, L. P., "Statistical OH-zone Structures of Turbulent Jet Flames from Liftoff to Near-Blowout," *Combust. Sci. and Tech.*, Vol. 79, pp. 311-324, 1991.
- Coats, C. M., and Zhao, H., "Transition and Stability of Turbulent Jet Diffusion Flames," *Twenty-Second Symposium (International) on Combustion*, The

- Combustion Institute, Pittsburgh, PA, pp. 685-692, 1988.
- Correa, S. M., "Relevance of Non-premixed Laminar Flames to Turbulent Combustion," Major Research Topics in Combustion, Hussaini, M. Y., Kumar, A., and Voigt, R. G., Eds., Springer-Verlag, pp. 45-69, 1992.
- Eichkoff, H., "Instability and Coherent Structures in Jet Flames," Recent Contributions to Fluid Mechanics, Hasse, Ed., Springer-Verlag, Berlin, 1982.
- Hanson, R. K., "Combustion Diagnostics: Planar Imaging Techniques," Twenty-first Symposium (International) on Combustion, The Combustion Institute, Pittsburgh, Pennsylvania, pp. 1677-1691, 1986.
- Hottel, H. C. and W. R. Hawthorne, "Diffusion in Laminar Flame Jets," Third Symposium (International) on Combustion, Flame and Explosive Phenomena, pp. 254-266, 1949.
- Karagozian, A. R., and Marble, R. E., "Study of a Diffusion Flame in a Stretched Vortex," Combust. Sci. and Tech., Vol. 45, pp. 65-84, 1986.
- Katta, V. R., Goss, L. P., and Roquemore, W. M., "Numerical Investigations on the Dynamic Behavior of a H<sub>2</sub>-N<sub>2</sub> Diffusion Flame under the Influence of Gravitational Force," AIAA Paper 92-0335, 1992.
- Knio, O. M. and Ghoniem, A. F., "Three Dimensional Vortex Simulation of Entrainment Augmentations Due to Streamwise Structures," AIAA Paper 89-0574, 1989.
- Laverdant, A. and Candel, S., "Combustion of Diffusion and Premixed Flames Rolled-up in Vortex Structures," AIAA J. Propulsion and Power, Vol. 5, p. 134, 1989.
- Lewis, G. S., "An Investigation of the Structure of a Laminar Non-Premixed Flame in an Unsteady Vortical Flow," Twenty-Second Symposium (International) on Combustion, The Combustion Institute, Pittsburgh, Pennsylvania, pp. 515-521, 1988.
- Lugt, J., "The Dilemma of Defining a Vortex," Theoretical and Experimental Fluid Mechanics, Muller, U., Rosner, F. G., and Schmidt, B., Eds., Springer-Verlag, 1979.
- Masri, A. R., R. W. Bilger, and R. W. Dibble, "Turbulent Nonpremixed Flames of Methane Near Extinction: Probability Density Functions," Comb. and Flame, 73, pp. 261-285, 1988.
- Poinson, T., Veynante, D. and Candel, S., "Quenching Processes and Premixed Turbulent Combustion Diagrams," J. Fluid Mech., Vol. 22, pp. 561-606, 1991.
- Post, M., Gord, J. and Goss, L. P., "Thin-Filament Pyrometry," To be presented in 31th Aerospace Sciences Meeting and Exhibit, AIAA, Reno Nevada, 1993.
- Roberts, W. L., Driscoll, J. F., Drake, M. C. Ratcliffe, J. W., Twenty-Fourth Symposium (International) on Combustion, The Combustion Institute, Pittsburgh, Pennsylvania, 1992, to appear.
- Roquemore, W. M., L.-D. Chen, L. P. Goss and W. F. Lynn, "Structure of Jet Diffusion Flames," Turbulent Reactive Flows, Lecture Notes in Engineering, Vol. 40, pp. 49-63, 1988.
- Rutland C., and Ferziger, J., "Interaction of a Vortex and a Premixed Flame," AIAA Paper 89-0127, 1989.
- Savas, O. and Gollahalli, S. R., "Flow Structure in the Near-Nozzle Region of Gas Jet Flames," AIAA Journal, Vol. 24, No. 7, pp. 1137-1140, 1986.
- Scholefield D. A., and J. E. Garside, "The Structure and Stability of Diffusion Flames," Third Symposium (International) on Combustion, Flame and Explosive Phenomena, pp. 102-110, 1949.
- Takahashi, F., M. Mizomoto and S. Ikai, "Transition from Laminar to Turbulent Free Jet Diffusion Flames," Comb. and Flame, Vol. 48, pp. 85-95, 1982.
- Takahashi, F., Schmoll, W. J., "Lifting Criteria of Jet Diffusion Flames," Twenty-Third Symposium (International) on Combustion, The Combustion Institute, Pittsburgh, Pennsylvania, 1991.
- Takahashi, F. and Goss L., "Near-Field Turbulent Structures and the Local Extinction of Jet Diffusion Flames," Twenty-fourth Symposium (International) on Combustion, The Combustion Institute, Pittsburgh, Pennsylvania, pp. 351-359, 1992.
- Takeno, T. and Kotani, Y., "Transition and Structure of Turbulent Jet Diffusion Flames," AIAA Paper 77-97, 1977.
- Vilimpoc, V. and Goss, L. P., "SiC-Based Thin Filament Pyrometry: Theory and Thermal Properties," Twenty-Second Symposium (International) on Combustion, The Combustion Institute, Pittsburgh, Pennsylvania, pp. 1907-1914, 1988.
- Wohl, K., Kapp, N. M., and C. Gazley, "Flame Stabilization and Quenching," Third Symposium (International) on Combustion, Flame and Explosive Phenomena, PP 3-21, 1949.
- Yule, A. J., Chigier, S. R., Boulderstone, R., and Ventura, J., "Combustion-Transition Interaction in a Jet Flame," AIAA Journal, pp. 725-760, 1981.

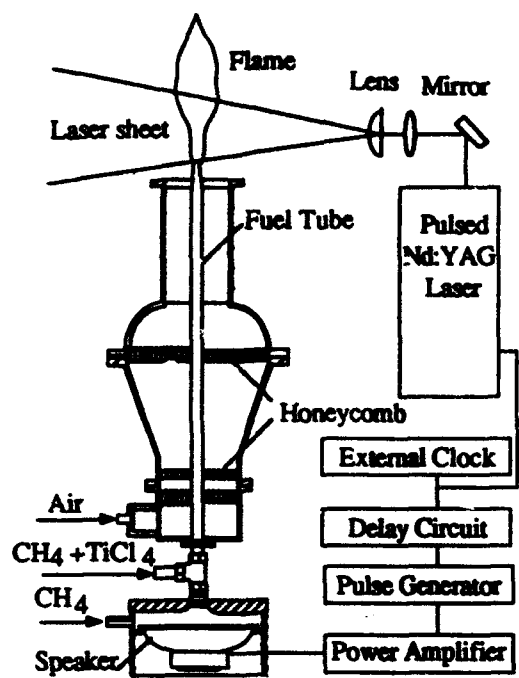


Figure 1. Schematics of Driven Diffusion Flame

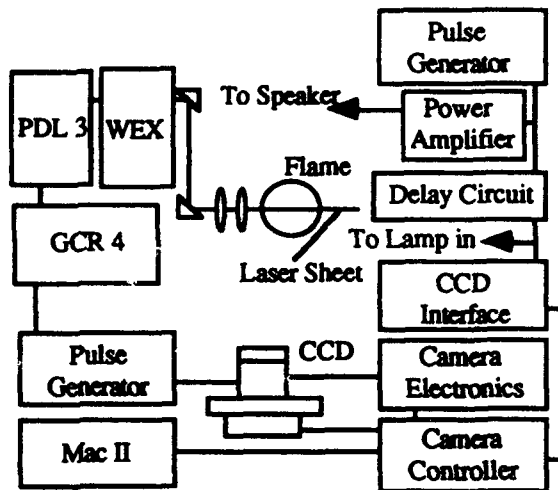


Figure 2. Experimental Setup of Phase-Locked Joint RMS and OH-PLIF Imaging

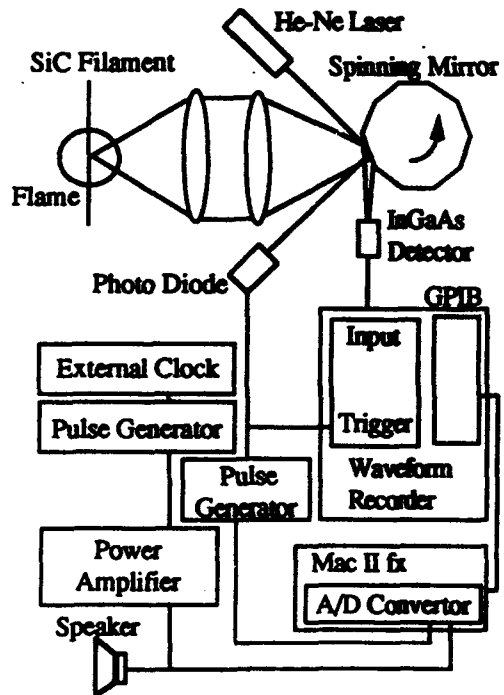


Figure 3. Experimental Setup of Thin-Filament Pyrometry Measurement

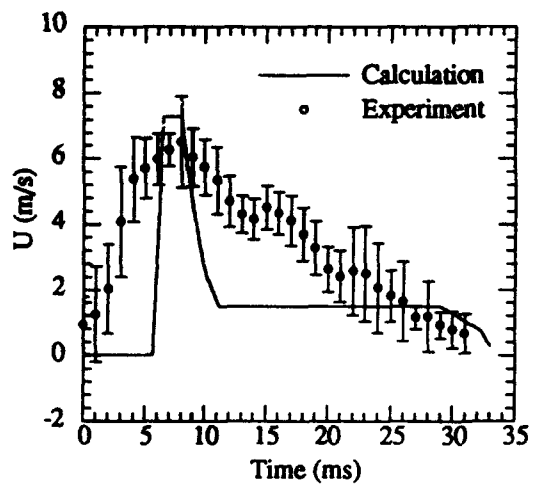
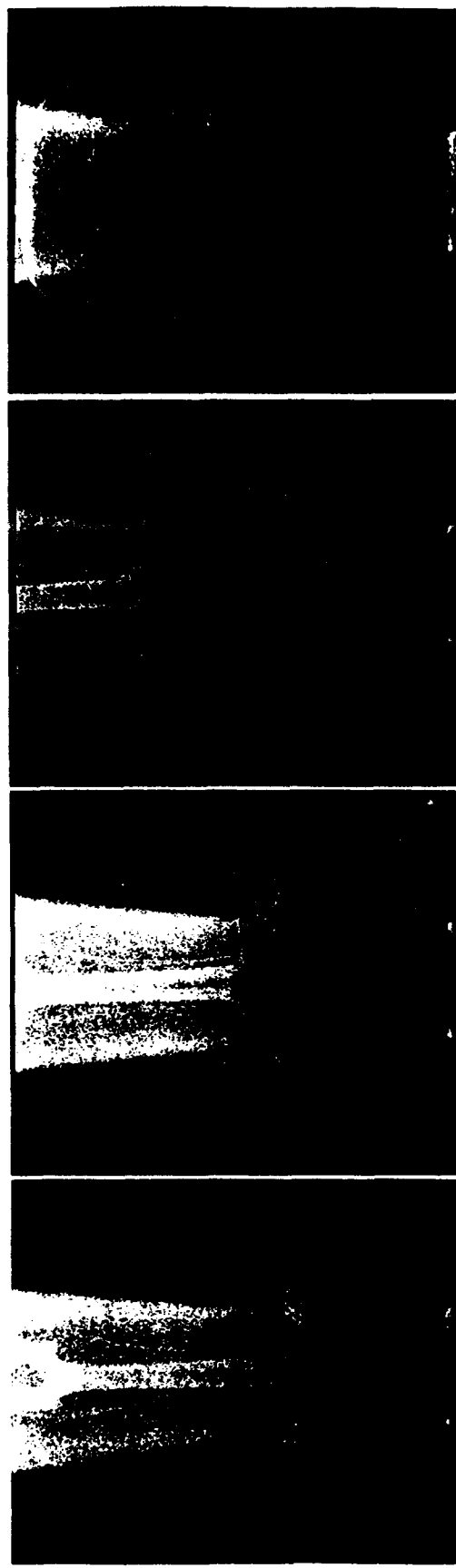
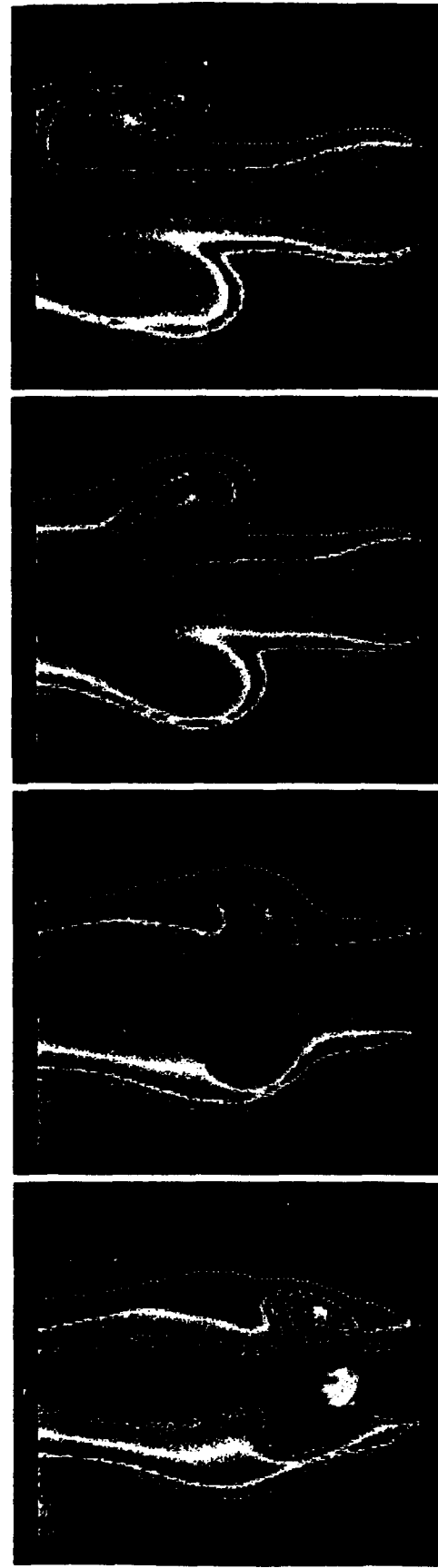


Figure 4. Time History of Axial Velocity Near the Centerline of the Nozzle Exit



(a)



(b)

Figure 5. The Evolution of Flame-Vortex Interaction by (a) reactive-Mie-scattering Flame Imaging, and (b) Time-dependent Numerical Simulation

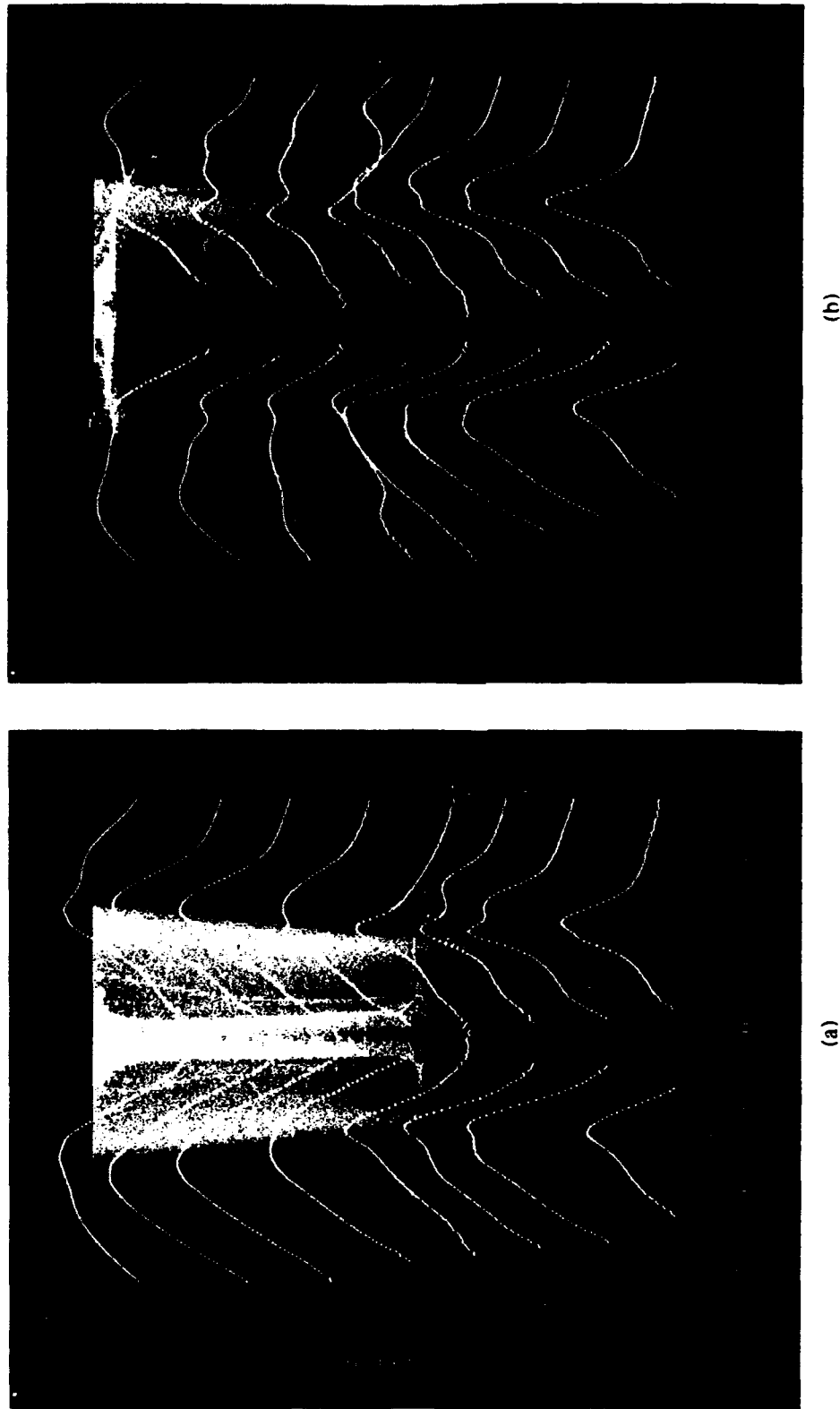


Figure 6. Composite Images of Flame and Phase-Averaged Temperature at (a)  $t = 10$  ms , and (b)  $t = 14$  ms

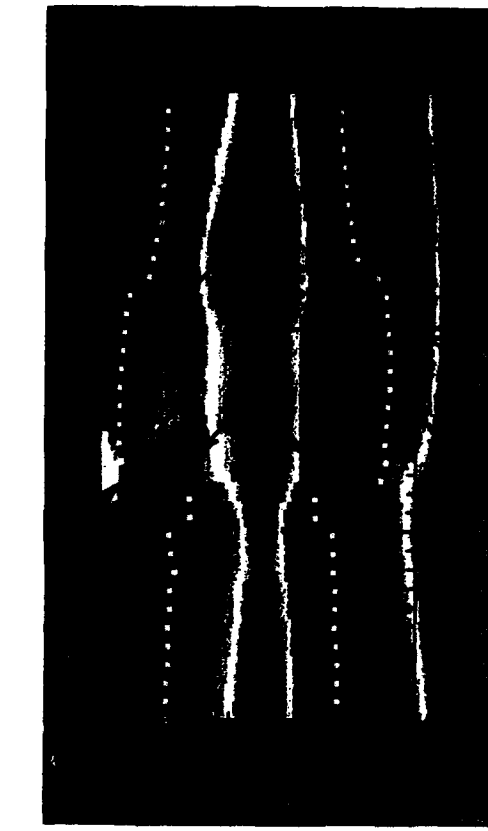


Figure 7. TFP Temperature Image and Locations of Peak Temperature  
( $z = 18$  mm)

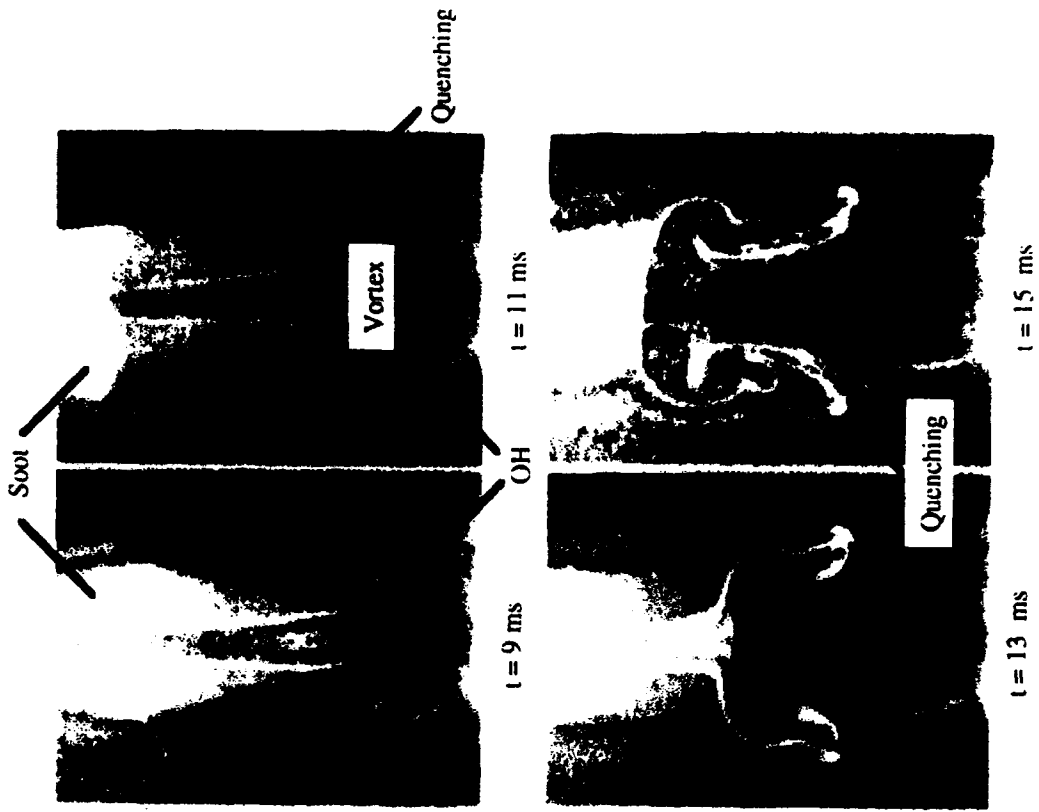


Figure 9. Joint RMS and OH-PLIF Images at Various Phase Angles  
( $z = 18$  mm)

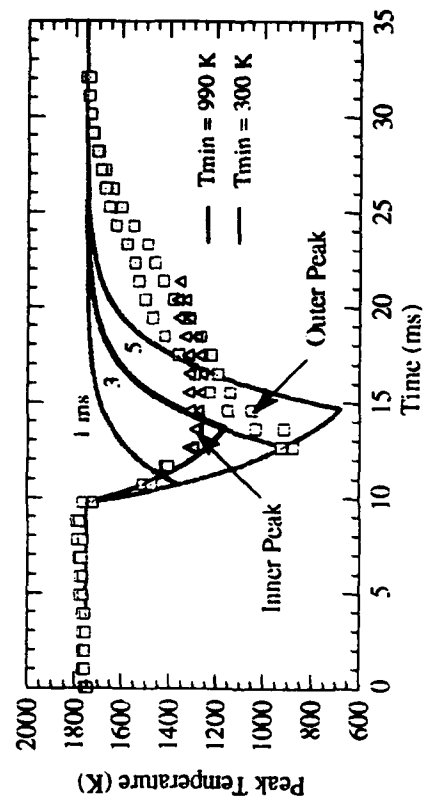
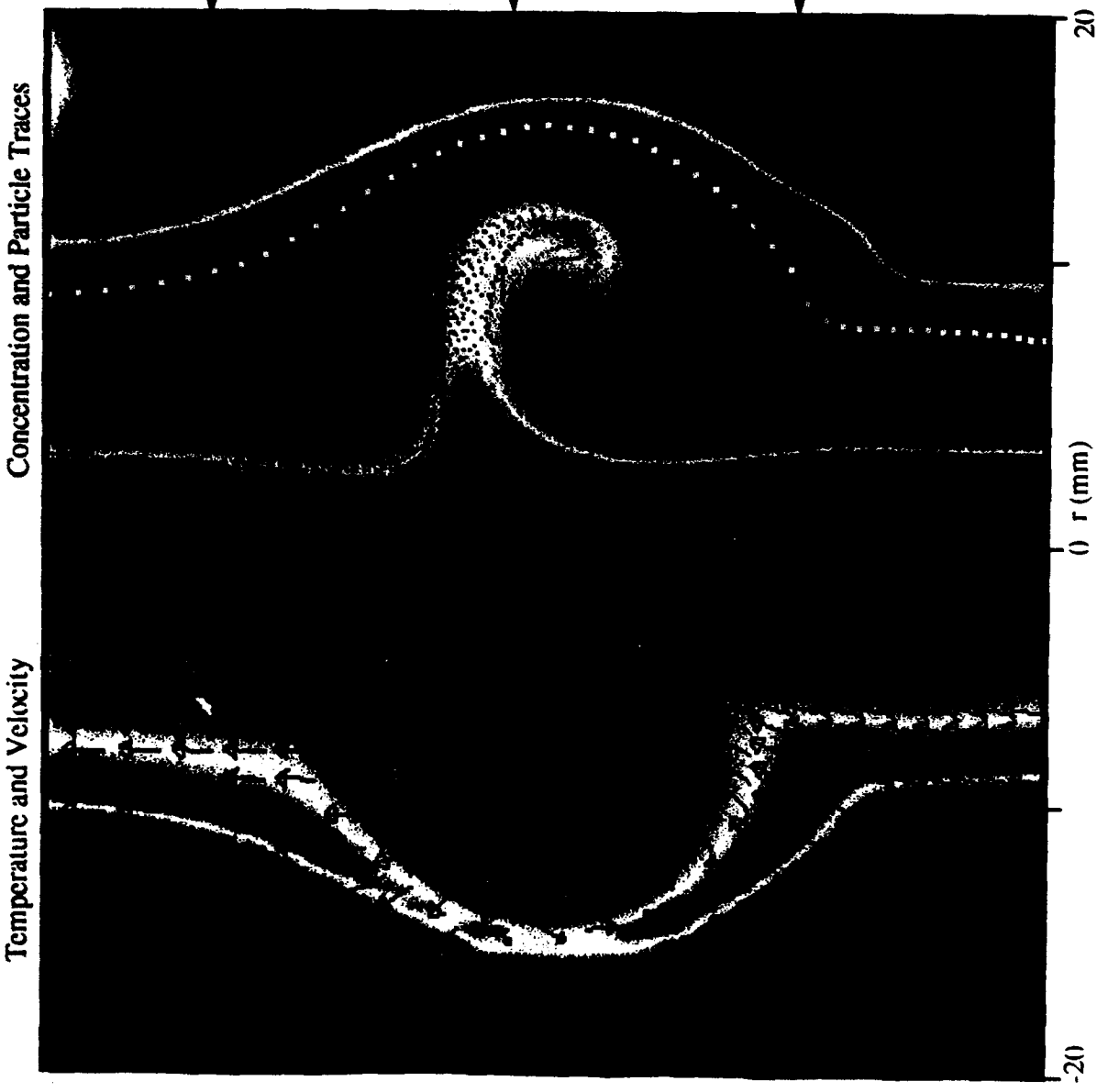


Figure 8. Peak Temperatures versus Time, and Filament Response  
( $z = 18$  mm)

### Temperature and Velocity



### Concentration and Particle Traces

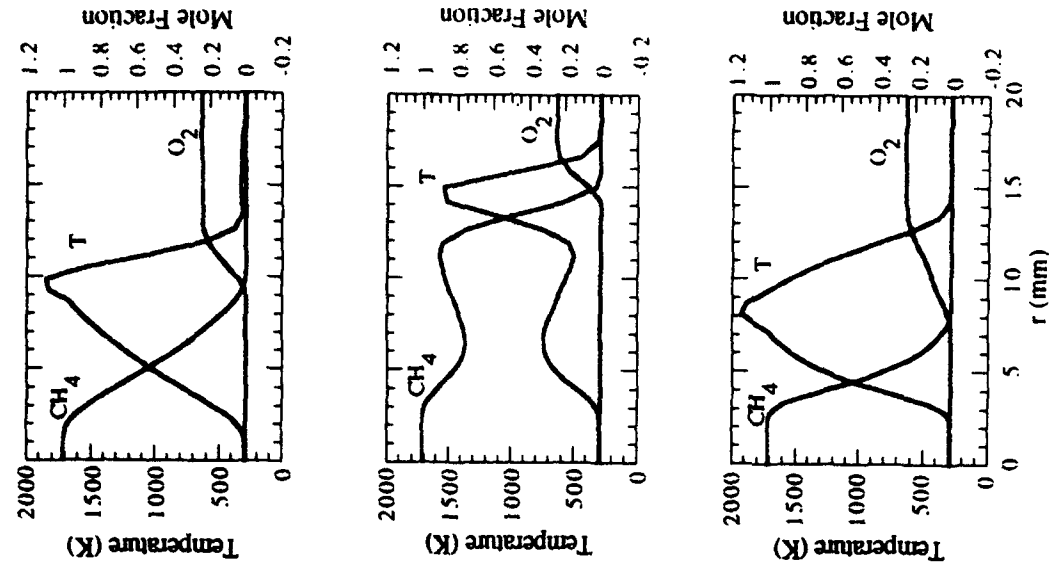


Figure 10. (a) Instantaneous Temperature and Concentration Fields with Superimposed Velocity Vectors and Particle Traces.  
 (b) Radial Profiles of Temperature, Mole Fractions of Fuel and Oxygen

(a)

(b)

**APPENDIX B**

**NUMERICAL INVESTIGATION OF A TRANSITIONAL JET DIFFUSION FLAME**

**VORTEX CROSSING FREQUENCY  
IN A TRANSITIONAL JET DIFFUSION FLAME**

**By**

**S. Lee,<sup>‡</sup> L.-D. Chen<sup>§</sup> and W. M. Roquemore<sup>¶</sup>**

<sup>‡</sup>Department of Mechanical Engineering  
The University of Iowa  
Iowa City, IA 52242

<sup>¶</sup>Aero Propulsion & Power Directorate  
Wright Laboratory  
WPAFB, OH 45433

**(To Be) Submitted To**

**COMBUSTION AND FLAME**

**Correspondence Should Be Addressed To**

**Professor Lea D. Chen  
Department of Mechanical Engineering  
The University of Iowa  
Iowa City, Iowa 52242**

**Phone: (319) 335-5674  
FAX: (319) 335-5669**

**??? 1994 ???**

## ABSTRACT

The crossing frequency of the inner vortex in a transitional jet diffusion flame is measured as a function of axial location using a line-visualization technique. The crossing frequency is the frequency for which the vortices are convected across a measurement line in a given height in the flame. Step-wise decreases of the crossing frequency are observed in the experiments, in qualitative agreement with that reported in the literature. The numerical simulation based on a simple flame-sheet model is shown to reproduce the inner vortex in the transitional jet diffusion flame studied. Random perturbations applied at the fuel jet exit are required for the prediction of the roll-up vortices inside the flame. The simulation results also reveal the step-wise decrease of the crossing frequency along the axial direction. The step decrease of the crossing frequency is shown to be a result of the vortex merging in jet diffusion flames. The simulation captures the major components of the crossing frequency in the near field; however, it is only in qualitative agreement with the experimental crossing frequency data as a function of axial location. The Strouhal number scaling of the vortex crossing frequency shows that the Strouhal number is bounded by 0.2 and 1.0, typical of the Kelvin-Helmholtz instability of cold jets. The present study suggests that the inner vortex is a Kelvin-Helmholtz type of the convective instability which is modified due to the presence of the high-temperature flame zone. The two-dimensional numerical model, therefore, is capable of reproducing the frequency characteristics of the buoyancy-induced vortex in transitional jet diffusion flames as well as capturing the frequency components of a Kelvin-Helmholtz type of instability inside the flame.

## INTRODUCTION

Two types of flow vortices are known to exist in transitional jet diffusion flames, the large toroidal vortex outside the stoichiometric surface (i.e., the outer vortex) and the small roll-up vortex inside (i.e., the inner vortex).<sup>1-4</sup> These vortices have been illustrated, for example, in our earlier flow/flame visualizations<sup>3-5</sup> using a light scattering technique known as the reactive Mie scattering (RMS). The visualization shows that the inner and outer vortices have different length scales, for example, centimeters for the outer vortex and millimeters for the inner vortex. The characteristic frequencies of these vortical structures are also different. The outer vortices are correlated with the flame flicker frequency,<sup>4,6</sup> typically in the range 10 to 20 Hz. The flame flicker is a consequence of the buoyancy acceleration as concluded in the numerical simulations of Ellzey and Oran<sup>7</sup> and Davis et al.<sup>8</sup> The microgravity combustion experiments of Bahadori et al.<sup>9</sup> also reported a stationary (non-oscillating) flame in reduced gravity. The buoyancy effects on flicker frequency have been quantified, for example, by Katta and Roquemore<sup>10</sup> and Sui,<sup>11</sup> showing that the flicker frequency is proportional to the square root of gravitational acceleration. This observation was in agreement with data compiled by Hamins et al.<sup>12</sup> in which the Strouhal number ( $St = \frac{vd}{u}$ , d the injector diameter, v the frequency, u the jet axial velocity) was found to be proportional to the square root of the Richardson number ( $Ri = \frac{gd}{u^2}$ , g the gravitational acceleration).

On the inner vortex, Yule et al.<sup>1</sup> quantified the crossing frequency in the near-injector region based on the high-speed Schlieren movies taken for non-premixed and partially-premixed flames of transitional jets. Their data showed that the crossing frequencies were typical about several hundred hertz and the frequency value differed from cold jets at a comparable  $Re_d$  ( $Re_d = \rho ud/\mu$ ;  $\rho$  the density and  $\mu$  the viscosity, properties based on jet-fluid at 298 K) condition. A step-wise decrease in vortex-crossing frequency along the axial direction was also observed. The coalescence and growth of inner vortices were identified to be responsible for the step-wise decrease in crossing frequency. In numerical simulations of the transitional jet diffusion flame, the inner and outer vortices were reproduced by Ellzey and Oran<sup>7</sup> and Katta and Roquemore.<sup>10</sup> Katta and Roquemore also illustrated that the buoyancy acceleration was important in the maintaining of

the coherence of the inner vortices. While the flame flicker frequency or the outer vortex has been characterized in the literature, the experimental data to quantify the inner vortex in transitional jet diffusion flames, however, are lacking. For example, comparison of the simulation with the experimental inner-vortex crossing frequency has not been reported. The objectives of this paper are (1) to extend the data base of the inner-vortex crossing frequency of a non-luminous diffusion flame and (2) to extend our earlier effort<sup>6</sup> of the time-accurate, two-dimensional simulation of transitional jet diffusion flames to compare the simulation with the experimental vortex crossing frequency.

## EXPERIMENTAL METHODS

A nonluminous jet diffusion flame was considered for the vortex-crossing frequency measurements. A H<sub>2</sub>/N<sub>2</sub> mixture with a molar ratio of 3.5 (molecular weight of 7.8) was used as fuel. The stoichiometric mixture fraction of this fuel is 0.126. The experiments were conducted in an unconfined, vertical combustion tunnel in the Air Force Wright Laboratory. This apparatus has been reported elsewhere;<sup>4-6</sup> therefore, only a brief description is given here. The burner section consisted of a vertically mounted fuel tube surrounded by an annular-air jet. The annular-air jet provided a low-speed coflow air, 0.16 m/s at the jet exit, to shield the jet diffusion flame from ambient disturbances. Two fuel nozzles of 5 and 10 mm in diameter were used. These fuel nozzles were made from a 25 mm stainless-steel tubing about 1 m long, with a tapered section (length about 100 mm) and a thin-wall nozzle lip (thickness less than 1 mm). Two fuel-jet exit velocities were examined, 7.8 and 23.0 m/s for d = 10 and 5 mm, respectively. The corresponding Reynolds numbers were 2300 and 3400.

The RMS visualization technique described in<sup>4-6,13</sup> was employed for planar and line visualizations. The planar visualization was for qualitative imaging of the vortex structures and the line visualization<sup>13</sup> was for quantitative crossing frequency measurements. A pulsed Nd:YAG laser (with the 532 nm output) was used as the light source for planar visualization. The image was recorded by an intensified CCD camera positioned at a right angle from the illuminating laser

sheet. The line visualization technique was described in.<sup>13</sup> A continuous-wave laser (an Ar<sup>+</sup> laser with 514.5 nm output) was positioned, passing through the center of the jet flame at axial heights of  $z/d = 0.41$  to  $6.24$  (10 mm nozzle) or  $2.8$  to  $12.5$  (5 mm nozzle) where  $z$  is the axial distance above the injector. A ten-facet rotating mirror was used to focus to a photomultiplier the light scattering from RMS particles ( $TiO_2$ ) along the laser beam, i.e., effectively scanning through the laser beam over the measuring "volume." The photomultiplier output was digitized by a high-speed digitizer (LeCroy TR8818) into 256 or 512 data blocks, i.e., 256 or 512 pixels per scan. The digitizer was operated at a speed in the range 4 to 6 MHz. The resultant spatial resolution for each pixel was better than  $200 \mu m$ . A He-Ne laser and a photodiode were used to trigger the digitizer during each scan of the mirror facet. The mirror rotational speed was set in the range 200 to 500 Hz, corresponding to an effective sweeping rate of 2 to 5 kHz. This sweeping (sampling) rate was adequate to quantify the vortex crossing frequency in this paper. A sampling period in the range 250 to 500 ms was taken for FFT (fast Fourier transform) analysis of the vortex crossing frequency.

## NUMERICAL METHODS

The explicit numerical scheme of Wu and Chen<sup>14</sup> was employed. This computer code is similar to that of Davis et al.<sup>8</sup>, except that a finite-volume formulation was used to replace the QUICKEST scheme and a different direct solver was used for the pressure Poisson equation. The computer program solves the time-dependent, axisymmetric Navier-Stokes equations coupled with the continuity and mixture fraction equations. The mathematical formulation is based on a flame sheet model. The major assumptions are an adiabatic flame, a one-step irreversible chemical reaction with  $H_2O$  being the only combustion product, an infinitely-large Damkohler number or an infinitely-thin reaction zone, equal diffusion coefficients for all species, a unity Lewis number, and a low Mach number, near-laminar, Newtonian flow with negligible radiative heat transfer and viscous dissipation. The present model is similar to that employed by Katta et al.<sup>15</sup> in the simulation of a similar  $H_2/N_2$  diffusion flame studied in this paper. The governing equations and

the boundary conditions will not be repeated here because they have been documented<sup>6,8</sup>, and in detail by Lee.<sup>16</sup>

The near-field development of a jet flow is known to be sensitive to the jet initial shear layer.<sup>17</sup> An initial momentum thickness of 0.21 mm using a hyperbolic-tangent profile<sup>18</sup> was specified. This momentum thickness was similar to that employed by Grinstein et al.,<sup>19</sup> and consistent with the measured thickness 0.3 mm determined from the LDA data.<sup>16</sup> The same shape of the hyperbolic-tangent profile was specified for the mixture fraction at the jet exit, with pure fuel having a value 1 and pure air a value 0. Small perturbation imposed to the axial velocity at the jet exit was necessary to initiate the roll-up of the inner vortices in the computation. A random number generator was used to introduce white noise at the fuel-jet exit, over a region of 4 to 8 grid points within 2 mm in the jet shear layer. The perturbation amplitude was set not to exceed 4 % of local velocity. The amplitude and the grids were randomly selected.

To resolve the small length scale associated with the inner vortex, 180 grid points were used for an axial distance of 600 mm and 80 grid points for a radial distance of 100 mm. The grids in the radial direction were concentrated in the shear layer region and around the stoichiometric surface. The grid spacing in axial direction was gradually increased as  $z$  was increased. The boundaries were set far from the stoichiometric surface to prevent the propagation of disturbance due to inaccuracies in specifying the boundary conditions of the finite computational domain. The time step was set to satisfy the Courant condition. Typically, a time step of 15  $\mu$ s or shorter was used. This time step was sufficient to resolve the evolution of the inner vortex. The computation was executed for 25,000 time steps for each condition considered. A computer workstation (Apollo DN 10000) was used, 15 CPU hours was required for 25,000 time steps (or 375 ms of real time).

## RESULTS AND DISCUSSION

The present injector yields "top-hat" velocity profiles at the burner exit as quantified by the LDA measurements.<sup>16</sup> These "top-hat" velocity profiles can be approximated by the hyperbolic-

tangent profiles used in the simulation. A typical RMS visualization of the flames studied is illustrated in Fig. 1. Both the outer and inner vortices can be seen in this visualization. The laser beam for line visualization was also illustrated (not scaled) in this figure. The line visualization of a similar flame with  $d = 10$  mm is shown in Fig. 2. Two flow structures were identified: outer and inner vortices, marked by scattered light from  $\text{TiO}_2$  particles outside or inside the stoichiometric surface. The outer vortex exhibits a crossing frequency of 15.6 Hz from the FFT analysis, cf. Fig. 3, in agreement with the 15 Hz flame-flicker frequency obtained for this flame using a laser-deflection technique.<sup>16,20</sup> The small cells are due to the crossings of the inner vortex visualized in the space-time coordinate of Fig. 2. These cells registered the signals from the discrete and finite-sized vortex when passing through a fixed line in space. A frequency around 420 Hz was obtained from the PSD (power spectral density) which was shown in Fig. 3. This crossing frequency was independent of the spatial location within the vortex cells. In general, interrogation over 25 pixels (or about 2 to 3 mm along the laser beam) was made to obtain the spectrum in the present study.

To assess whether the numerical simulation can reproduce the crossing frequency of the inner vortex, the line visualization of the simulation is shown in Fig. 4 for the condition of Fig. 2, using the predicted radial velocity. The line visualization of the simulation showed the crossings of the inner vortex, marked by the cells in the time-space coordinate. This visualization was similar to the experimental observation. The simulation also showed that the vortex crossing frequency was independent of spatial locations when the interrogation was taken within the cells. Specifically for  $d = 10$  mm, the predominant frequency was nearly identical for  $0.29 < r/d < 0.71$  ( $r$  the radial distance), consistent with the experimental observation. A standard location at  $r = 3.98$  mm was chosen for analysis of the simulation results. The line visualization also showed that the vortex cell grows in size at downstream locations. At downstream locations, the crossing frequency seems to have decreased.

To compare the PSD at different axial locations, Fig. 5 summarized the experimental and simulation results at three axial locations. Different vortex crossing frequencies were found in the spectrum. For example, the measurements revealed two major components centered around 460

Hz and 840 Hz at  $z/d = 2.0$ , one component around 490 Hz at  $z/d = 4.0$  and 320 Hz at  $z/d = 5.1$ . At  $z/d = 4.0$  and 5.1, the flicker frequency around 15 Hz was also registered. The simulation showed that the vortex crossing frequency peaked around 400 Hz at  $z/d = 2.0$  and 300 Hz at  $z/d = 3.6$  and  $z/d = 4.9$ . The flame flicker frequency around 15 Hz was also predicted in the simulation. These PSD's showed that the vortex crossing frequency decreases as axial distance is increased.

To assess whether the step change described by Yule et al.<sup>1</sup> also exists in the flame studied, the inner vortex crossing frequency was plotted as a function of  $z/d$  in Fig. 6. The strongest component in the spectrum other than the flicker frequency was taken as the crossing frequency. Indeed, step change was evident. For example, the measured frequency decreased from 1400 Hz to 850 Hz at  $z/d = 1$ , to 450 Hz at  $z/d = 2$ , and to 300 Hz at  $z/d = 5$ . At  $z/d = 6$ , there seems to be another step change of the frequency from 300 Hz to 250 Hz, although this change is not as evident as the above-noted decreases. The numerical simulation also predicted a similar step decrease in the crossing frequency. The simulation consistently underestimated the vortex crossing frequency, although the discrepancy was reduced at downstream locations. The comparison was not extended to downstream locations because the inner vortex has become three-dimensional at  $z/d$  around 8. The results of the vortex crossing frequency in the 5 mm diffusion flame are similar to the 10 mm flame and step-wise decreases are also observed.<sup>16</sup>

To assist the interpretation of step decrease of the crossing frequency, the predicted time trace of radial velocity at four axial heights is shown in Fig. 7 for the 10 mm flame. The velocity at the near-injector exit ( $z/d = 0.93$ ) appeared to be noisy; the periodicity in the signal was not obvious. A "modulation" or "merging" of the signal into a more periodic time trace seems to have occurred at downstream locations. For example, the time trace merged into six cycles at  $z/d = 0.93$  over the time period 9 to 12 ms (cf., Fig. 7), into two cycles at  $z/d = 1.54$  over 10 to 13 ms, and into a single cycle at  $z/d = 3.12$  over 13 to 16 ms. The time-trace results suggested that the vortex merging was responsible for the step decrease of the crossing frequency. The vortex merging in transitional jet diffusion flames has been identified, for example, in RMS visualizations.<sup>3,4</sup> The vortex merging or step-wise frequency decrease in jet diffusion flames is similar to the vortex

pairing (or period doubling) of the cold jets.<sup>21</sup> The merging process in jet diffusion flames, however, is different from cold jets. A step-wise decrease, not equal to the frequency halving of the cold jets, was typical in jet diffusion flames. The jet diffusion flame also has a complex spectrum showing a broad-band around the predominant frequency (cf., Fig. 5) while a simple and well defined peak is typical for cold jets.<sup>16</sup> The broadening of the spectrum is due to the presence of the high-temperature flame zone which limits the growth of the inner vortex. The vortex-crossing frequency is further complicated by the time-varying flame zone due to the buoyant instability (and other sources) and the accompanied time-varying velocity. As a result, a more complex spectrum is typical for the jet diffusion flame compared to the cold jet at a similar  $Re_d$  condition.

The Strouhal number has been used in the scaling of the Kelvin-Helmholtz instability in non-reacting jets.<sup>17,18</sup> The Strouhal based on the injector diameter ( $St_d$ ) was plotted as a function of  $Re_z$  (based on axial distance) in Fig. 8, including three more data sets of simulation results. All the conditions in Fig. 8 have a  $Re_d$  in the range 2300 to 3400. The results showed that the  $St_d$  was generally in the range 0.2 to 1.0, and  $St_d$  decreased as  $Re_z$  was increased. A nearly constant value around 0.2 was found for  $Re_z$  in the range 50,000 to 60,000. The  $St_d$  of 0.2 was typical for a non-reactive jet with a thin initial shear layer (or a top-hat velocity profile). When the momentum thickness ( $\theta$ ) was used as the length scale,  $St_\theta$  was shown to be bounded by 0.005 and 0.05 for the conditions examined.<sup>16</sup> These observations, along with the fact that a random perturbation was needed for simulation of the inner vortex, the inner vortex appears to be a Kelvin-Helmholtz type of the convective instability modified due to the presence of a high temperature flame zone.

## SUMMARY AND CONCLUSIONS

The crossing frequency of the inner vortex in a transitional jet diffusion flame (with a near "top-hat" velocity profile at the burner exit) is studied. The crossing frequency has been measured for two nitrogen-diluted hydrogen jet diffusion flames, employing a line visualization technique. Spatially-resolved vortex crossing frequencies are documented. Step-wise decreases of the

crossing frequency are observed for the conditions examined, in qualitative agreement with Yule et al.<sup>1</sup> The numerical simulation based on a simple flame-sheet model is shown to be capable of reproducing the outer and the inner vortices in the flame studied. Random perturbation imposed to the axial velocity, however, is needed at the fuel jet exit to initial the roll-up of the inner vortices. The simulation also reveals step-wise decreases of the crossing frequency along the axial direction. The step decrease of the crossing frequency has been shown to be a result of the vortex merging in jet diffusion flames. The broad-band spectrum is believed to be due to the presence of the flame zone. The predicted crossing frequencies, although are only in qualitative agreement with the spatially-specific experimental data, do capture the major components in the near field of the flame.

The Strouhal number scaling of the vortex crossing frequency (based on the jet diameter) versus the Reynolds number based on axial distance shows that the Strouhal number is bounded by 0.2 and 1.0, typical of the Kelvin-Helmholtz instability of cold jets. This fact along with simulation requiring a perturbation source at the jet exit (which was not needed for the buoyant instability<sup>6</sup>) suggests that the inner vortex is a Kelvin-Helmholtz type of the convective instability, and the instability was modified due to the presence of the high-temperature flame zone. Further validation of this hypothesis, however, is needed. The present study, in our opinion, represents a significant advancement in our effort to verify the two-dimensional, time-accurate prediction of transitional jet diffusion flames. The numerical model is shown not only it can reproduce the frequency characteristics of the buoyancy-induced vortex in transitional jet diffusion flames<sup>6</sup> but also it can capture the frequency components of a Kelvin-Helmholtz type of instability inside the flame.

There are several limitations in the present numerical model, for example, the unity Lewis number assumption and the two-dimensional simulation. The non-unity Lewis number effect has been shown to alter the local temperature due to the preferential diffusion in the flame studied,<sup>22</sup> but it did not alter the global dynamics of the flame. To what extent the preferential diffusion affects the time characteristics of the inner vortex is yet to be ascertained. To apply the time-

accurate calculation for highly three-dimensional turbulent flames, of course, remains a continued challenge to the authors.

#### **ACKNOWLEDGMENT**

This work was supported by the Air Force Aerospace Sciences Directorate of AFOSR. The assistance of Dr. L. P. Goss in conducting the line-visualization measurements is gratefully acknowledged. The U. S. Government is authorized to reproduce and distribute copies for governmental purposes notwithstanding any copyright notation hereon.

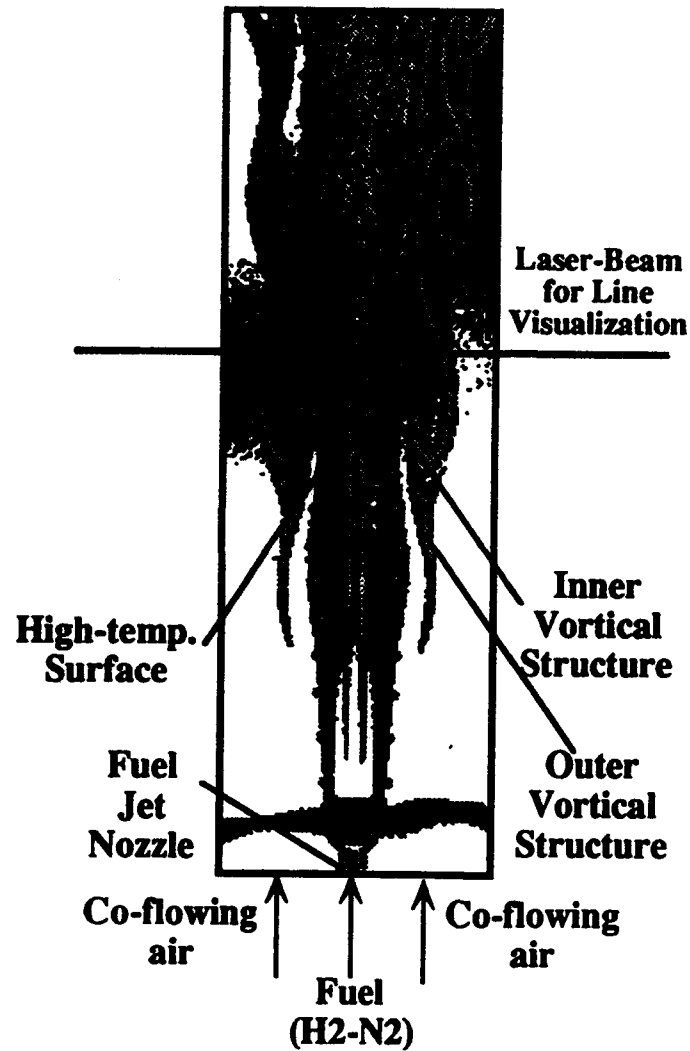
## REFERENCES

1. Yule, A. J., Chigier, N. A., Ralph, S., Boulderstone, R., and Ventura, J., *AIAA J.* 19:752 (1981).
2. Eickhoff, H., in *Recent Contributions to Fluid Mechanics*, Springer-Verlag, 1982.
3. Roquemore, W. M., Chen, L.-D., Goss, L. P., and Lynn, W. F., in *Turbulent Reactive Flows, Lecture Notes in Engineering* (R. Borghi and S. N. B. Murthy, Eds.), Springer-Verlag, Berlin, 1989, Vol. 40, p. 49.
4. Chen, L.-D., Seaba, J. P., Roquemore, W. M., and Goss, L. P., *Twenty-Second Symposium (International) on Combustion*, The Combustion Institute, Pittsburgh, 1988, pp. 677-684.
5. Chen, L.-D. and Roquemore, W. M., *Combustion and Flame* 66:81-86 (1986).
6. Chen, L.-D., Vilimpoc, V., Goss, L. P. Davis, R. W., Moore, E. F., and Roquemore, W. M., *Twenty-Fourth Symposium (International) on Combustion*, The Combustion Institute, pp. 303-310, 1992
7. Ellzey, J. L. and Oran, E. S., *Twenty-Third Symposium (International) on Combustion*, The Combustion Institute, Pittsburgh, 1990, pp. 1635-1640.
8. Davis, R. W., Moore, E. F., Chen, L.-D., Vilimpoc, V., Goss, L. P. and Roquemore, W. M., *Combustion and Flame* 83:263-270 (1991).
9. Bahadori, M. Y., Edelman, R. B., Stocker, D. P., and Olson, S. L., *AIAA Journal* 28:236-244 (1990).
10. Katta, V. R. and Roquemore, W. M., *Combustion and Flame* 92:274-282 (1993).
11. Sui, P.-C., "Propane Buoyant Jet Diffusion Flame," M.S. Thesis, Department of Mechanical Engineering, The University of Iowa, Iowa City, 1992.
12. Hamins, A., Yang, J. C., and Kashiwagi, T., *Twenty-fourth Symposium (International) on Combustion*, The Combustion Institute, pp. 1695-1702, 1992.

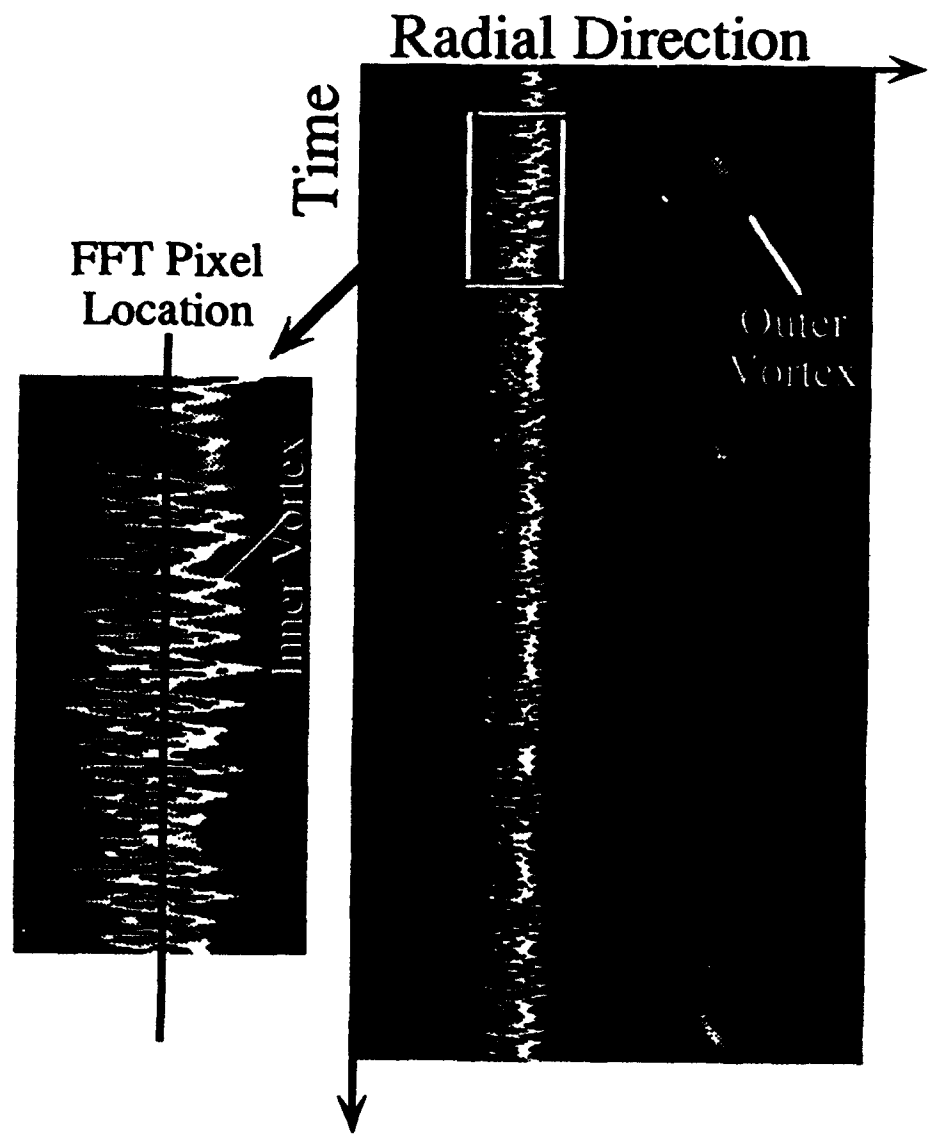
13. Takahashi, F. and Goss, L. P., *Twenty-Fourth Symposium (International) on Combustion*, The Combustion Institute, pp. 351-359, 1992.
14. Wu, S.-H. and Chen, L.-D., *AIAA J. Prop. Power* 8 (5): 921-926 (1992).
15. Katta, V. R., Goss, L. P. and Roquemore, W. M., *AIAA Paper No. 92-0335* (1992).
16. Lee, S., Flow-Flame Interaction OF Nitrogen-diluted Hydrogen Jet Diffusion Flame, Ph.D. Dissertation, Department of Mechanical Engineering, The University of Iowa, Iowa City, 1992.
17. Ho, C.-M. and Huerre, P., *Annual Review of Fluid Mechanics* 16: 365-424 (1984).
18. Michalke, A., *Prog. in Aerospace Sci.* 21: 159-199 (1984).
19. Grinstein, F. F., Oran, E. S., and Boris, J. P., *AIAA J.* 25: 92-97 (1987).
20. Lee, S., Chen, L.-D., Roquemore, W. M., and Goss, L. P., in *Proceedings of the 1991 Central States Section Spring Technical Meeting of The Combustion Institute*, The Combustion Institute, 1991, pp. 119-124.
21. Zaman, K. B. M. Q., and Hussain, A. K. M. F., *J. Fluid Mech.* 101:449-491 (1980).
22. Katta, V. R., private communication (1993)

## LIST OF FIGURES

- Fig. 1. RMS visualization of a H<sub>2</sub>/N<sub>2</sub> jet diffusion flame ( $u_j = 23.5$  m/s,  $d = 5$  mm,  $Re_d = 3400$ ;  $u_a = 0.16$  m/s);  $u_j$  the fuel-jet exit velocity,  $d$  the diameter,  $Re_d$  the jet exit Reynolds number and  $u_a$  the coflow annular air velocity at the jet exit; the image view was about 65 mm (radial) by 200 mm (axial); the high temperature surface was inferred from thin-filament visualization measurements.<sup>16</sup>
- Fig. 2. Line visualization of a H<sub>2</sub>/N<sub>2</sub> jet diffusion flame ( $u_j = 7.8$  m/s,  $d = 10$  mm,  $Re_d = 2300$ ;  $u_a = 0.16$  m/s); the laser beam was located at  $z/d = 4.7$ , and the mirror scanning rate was set at 4 kHz and the digitizing rate at 6 MHz.
- Fig. 3. The PSD of data shown in Fig. 2.
- Fig. 4. Line visualization of the numerical simulation a H<sub>2</sub>/N<sub>2</sub> jet diffusion flame ( $u_j = 7.8$  m/s,  $d = 10$  mm,  $Re_d = 2300$ ;  $u_a = 0.16$  m/s).
- Fig. 5. The PSD of a H<sub>2</sub>/N<sub>2</sub> jet diffusion flame ( $u_j = 7.8$  m/s,  $d = 10$  mm,  $Re_d = 2300$ ;  $u_a = 0.16$  m/s) due to the inner vortex crossing (a) experimental data at  $z/d = 2.0, 4.0$  and  $5.1$ , and (b) simulation results at  $z/d = 2.0, 3.6$  and  $4.9$ .
- Fig. 6. The vortex crossing frequency of a H<sub>2</sub>/N<sub>2</sub> jet diffusion flame ( $u_j = 7.8$  m/s,  $d = 10$  mm,  $Re_d = 2300$ ;  $u_a = 0.16$  m/s) as a function of  $z/d$ ; experimental data shown by closed symbols, simulation by open symbols.
- Fig. 7. The time trace of radial velocity at different axial locations of a H<sub>2</sub>/N<sub>2</sub> jet diffusion flame ( $u_j = 7.8$  m/s,  $d = 10$  mm,  $Re_d = 2300$ ;  $u_a = 0.16$  m/s); the circled regions illustrate the evolving (or modulation) of the time trace into periodical signals.
- Fig. 8. Scaling of the crossing frequency by the Strouhal number based on nozzle diameter,  $St_d$ , versus the Reynolds number based on axial location  $Re_z$ , for different flow conditions and different axial locations; \* denotes experimental measurements.

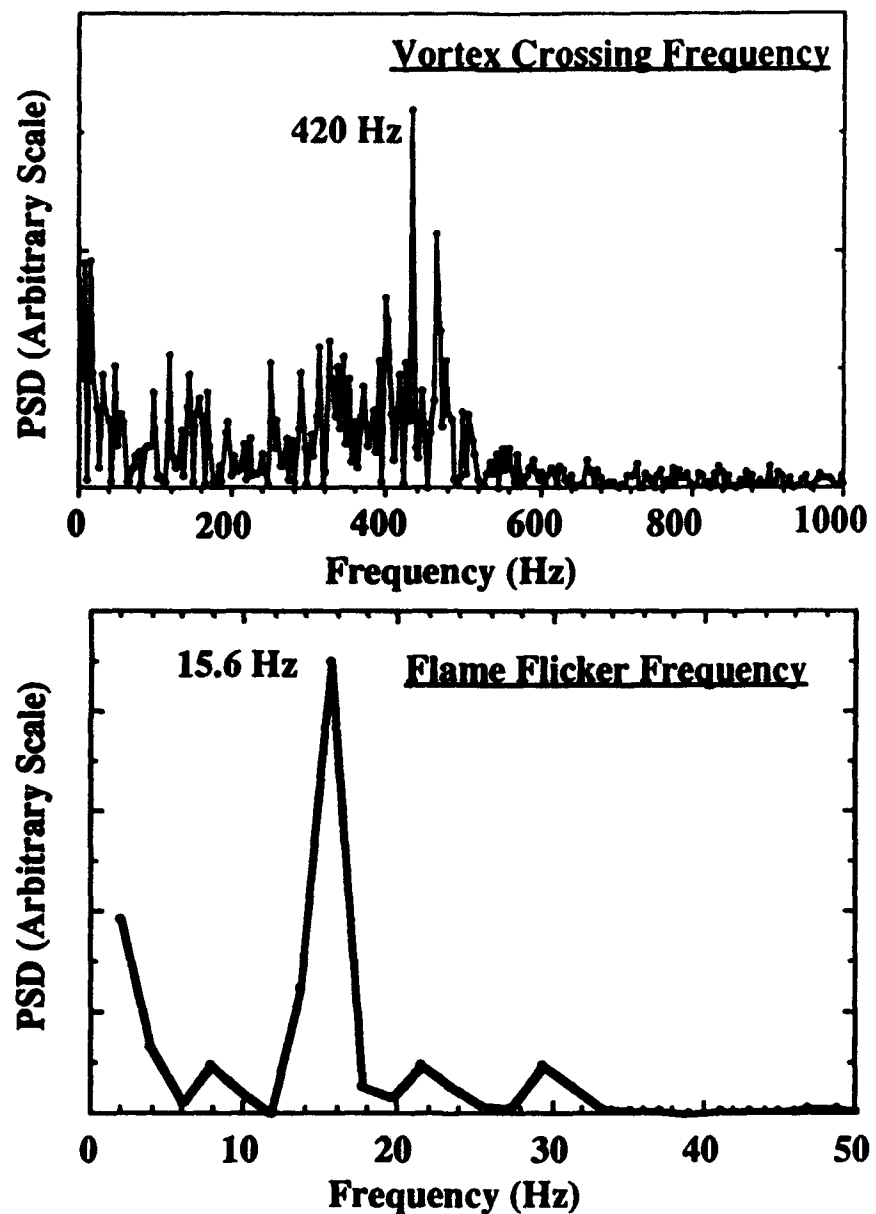


Lee, Chen, Rogerson  
Fig. 1

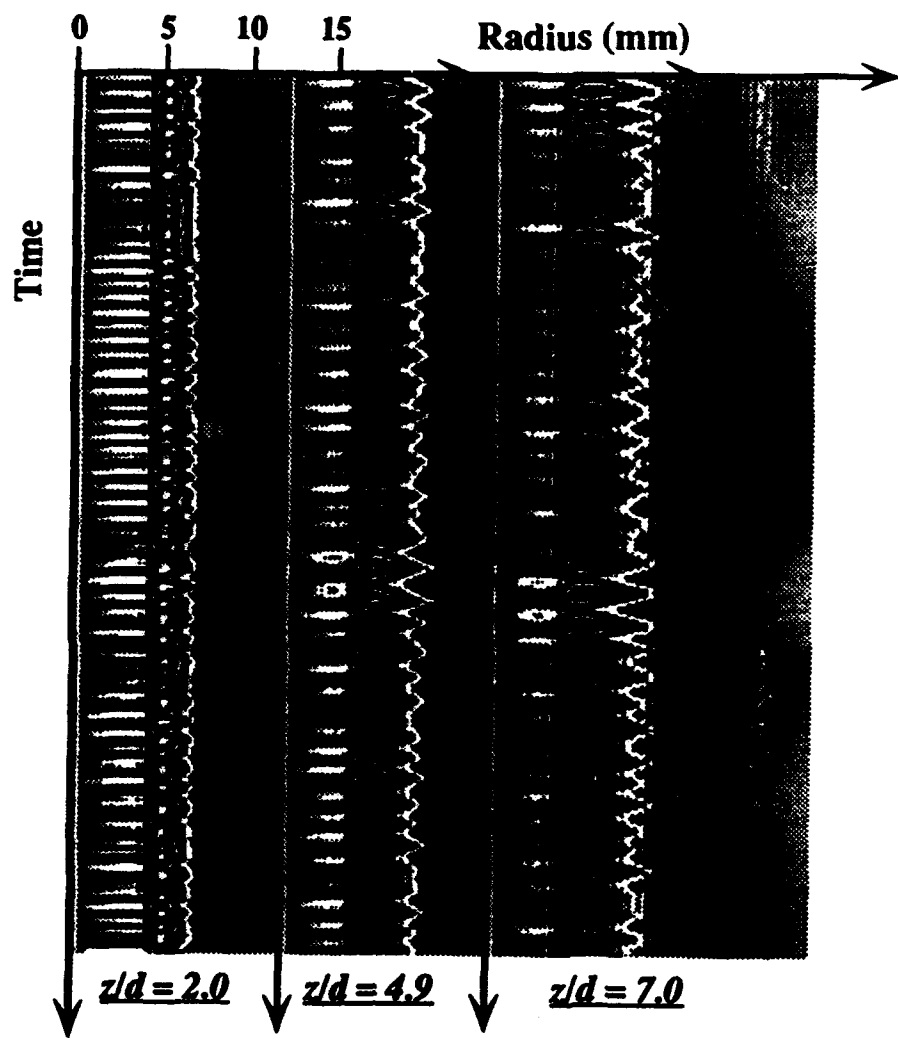


Lee, Chen, Rogerson

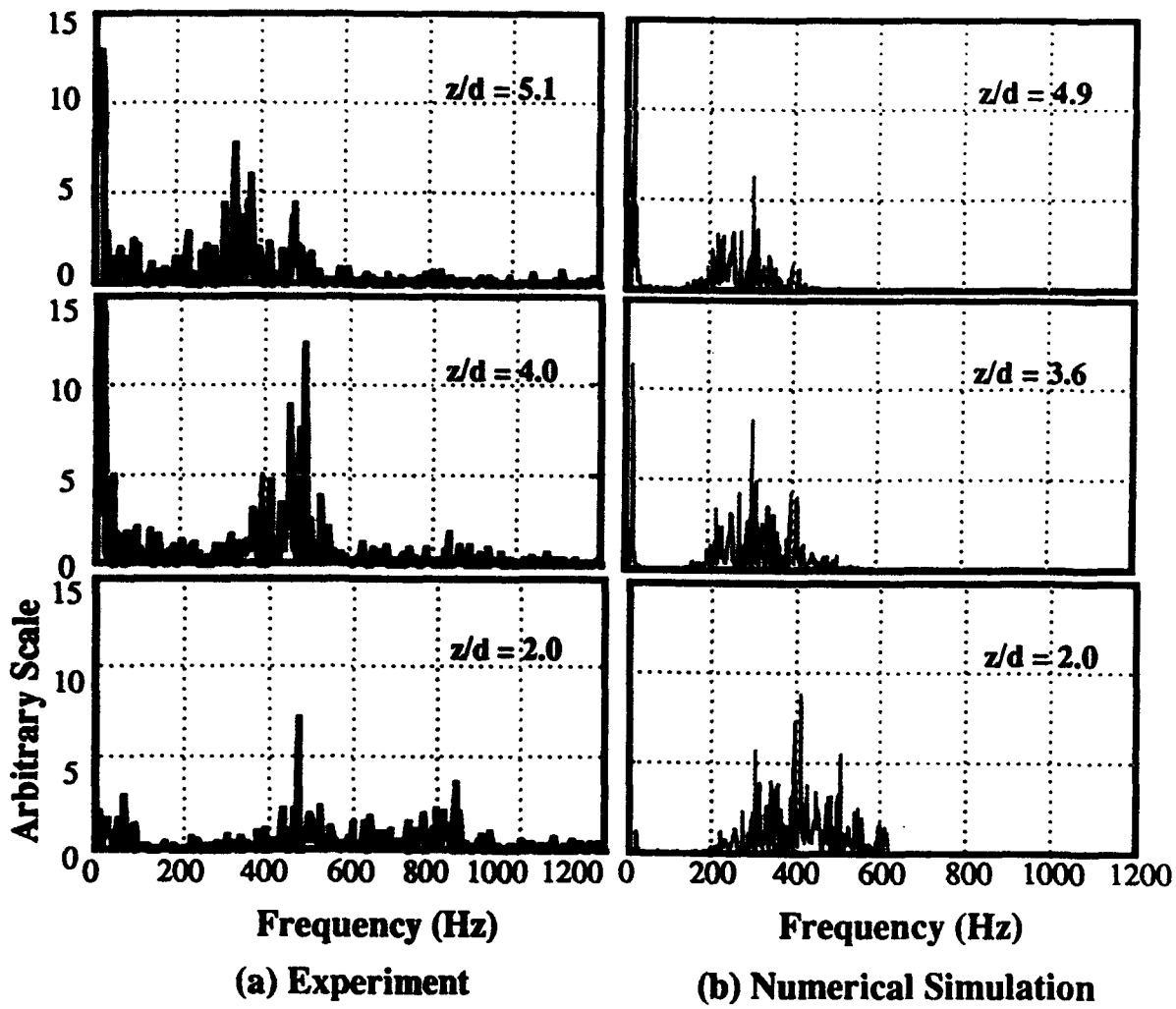
Fig. 2



Lee, Chen, Rogerson  
Fig. 3

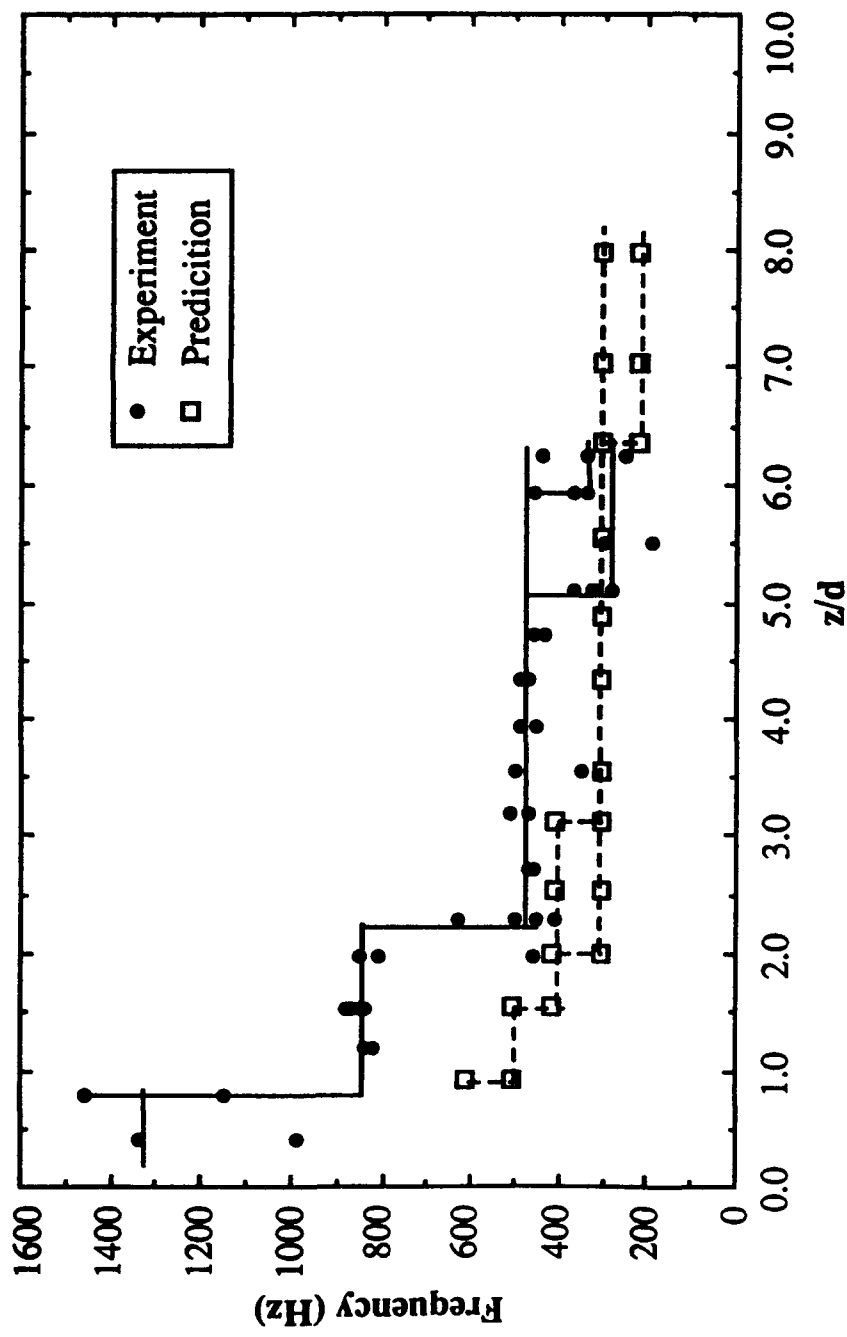


Lee, Chen, Rogozenok  
Fig. 4



Lee, Chien, Roquemore

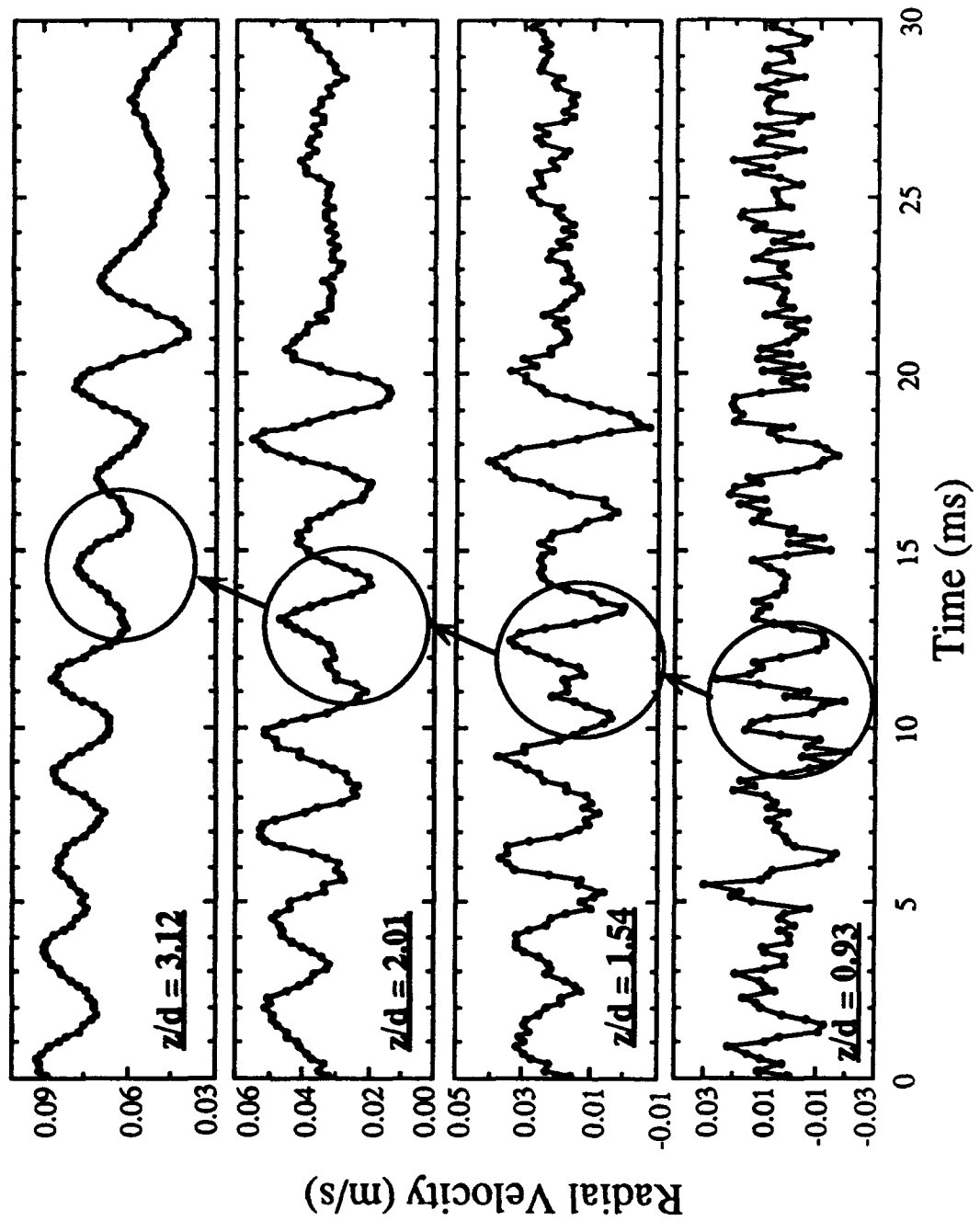
Fig. 5

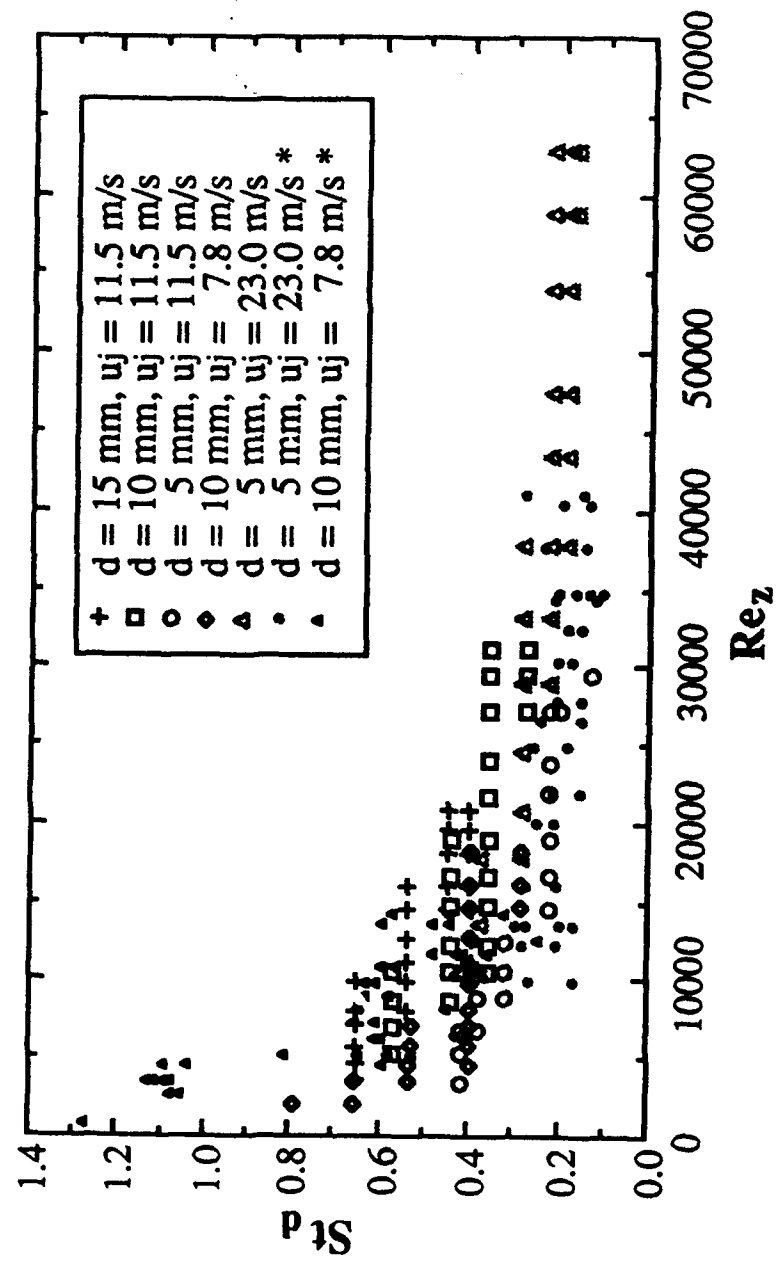


Lee, Chen, Roquemore

Fig. 6

Laser velocimetry





مکالمہ احمدیہ